







Impaired disassembly of the axon initial segment restricts mitochondrial entry into damaged axons

Sumiko Kiryu-Seo^{1,*} , Reika Matsushita¹, Yoshitaka Tashiro^{2,†}, Takeshi Yoshimura^{3,4} , Yohei Iguchi⁵, Masahisa Katsuno⁵ , Ryosuke Takahashi² & Hiroshi Kiyama^{1,**} 

Abstract

The proteasome is essential for cellular responses to various physiological stressors. However, how proteasome function impacts the stress resilience of regenerative damaged motor neurons remains unclear. Here, we develop a unique mouse model using a regulatory element of the activating transcription factor (Atf3) gene to label mitochondria in a damage-induced manner while simultaneously genetically disrupting the proteasome. Using this model, we observed that in injury-induced proteasome-deficient mouse motor neurons, the increase of mitochondrial influx from soma into axons is inhibited because neurons fail to disassemble ankyrin G, an organizer of the axon initial segment (AIS), in a proteasome-dependent manner. Further, these motor neurons exhibit amyotrophic lateral sclerosis (ALS)-like degeneration despite having regenerative potential. Selectively vulnerable motor neurons in SOD1^{G93A} ALS mice, which induce ATF3 in response to pathological damage, also fail to disrupt the AIS, limiting the number of axonal mitochondria at a pre-symptomatic stage. Thus, damage-induced proteasome-sensitive AIS disassembly could be a critical post-translational response for damaged motor neurons to temporarily transit to an immature state and meet energy demands for axon regeneration or preservation.

Keywords axonal transport; nerve injury; neurodegenerative disease; organelle; stress response

Subject Categories Molecular Biology of Disease; Neuroscience; Organelles

DOI 10.15252/embj.2021110486 | Received 5 January 2022 | Revised 15 July 2022 | Accepted 20 July 2022 | Published online 25 August 2022

The EMBO Journal (2022) 41: e110486

Introduction

Nerve-injured motor neurons can regenerate through multiple stress responses, which require dynamic protein synthesis and degradation (Kiryu-Seo & Kiyama, 2011; Patodia & Raivich, 2012). The proteasome is thought to be involved in the post-translational stress response of damaged motor neurons; however, it remains unclear how proteasome function impacts the stress resilience of damaged motor neurons. Proteasomal dysfunction in motor neurons has been implicated in the pathology of amyotrophic lateral sclerosis (ALS) (Kabashi *et al*, 2012; Webster *et al*, 2017), a progressive neurodegenerative disease characterized by motor neuron loss, neuromuscular denervation, and axon degeneration (Taylor *et al*, 2016; Nijssen *et al*, 2017). Intriguingly, multiple stress responses observed in injured motor neurons are similarly activated in pathologically damaged motor neurons of ALS model mice (Kiryu-Seo *et al*, 2005; Lobsiger *et al*, 2007; Sun *et al*, 2015; Tyzack *et al*, 2017; Maor-Nof *et al*, 2021). We hypothesized that a proteasome-mediated stress-resilient mechanism exists in regenerative damaged motor neurons, which is lacking in damaged motor neurons prior to degeneration.

Alteration of axonal mitochondrial dynamics in response to damage is an early hallmark of both regeneration and degeneration (Patron & Zinsmaier, 2016; Sleigh *et al*, 2019). Mitochondria play pivotal roles in energy supply and metabolism that depend on cellular status (Han *et al*, 2020; Licht-Mayer *et al*, 2020). In neurons with long axons, such as motor neurons, mitochondria must be transported from the cell body to the axon. It is evident that successful regeneration requires enhanced transport and numbers of mitochondria in injured axons (Misgeld *et al*, 2007; Kiryu-Seo *et al*, 2010, 2016; Cartoni *et al*, 2016; Han *et al*, 2016). Increases in motile mitochondria or deletion of stationary mitochondria in injured axons can facilitate axon regeneration (Zhou *et al*, 2016; Han *et al*, 2020). Dysregulation of mitochondrial transport and quality has been observed during the very early onset of ALS

1 Department of Functional Anatomy and Neuroscience, Nagoya University Graduate School of Medicine, Nagoya, Japan

2 Department of Neurology, Kyoto University Graduate School of Medicine, Kyoto, Japan

3 Department of Child Development and Molecular Brain Science, United Graduate School of Child Development, Osaka University, Osaka, Japan

4 Department of Neuroscience, Baylor College of Medicine, Houston, TX, USA

5 Department of Neurology, Nagoya University Graduate School of Medicine, Nagoya, Japan

*Corresponding author. Tel: +81 52 744 2015; Fax: +81 52 744 2027; E-mail: skiryu@med.nagoya-u.ac.jp

**Corresponding author. Tel: +81 52 744 2015; Fax: +81 52 744 2027; E-mail: kiyama@med.nagoya-u.ac.jp

†Present address: Department of Aging Neurobiology, Center for Development of Advanced Medicine for Dementia, National Center for Geriatrics and Gerontology, Aichi, Japan

degeneration (Bilsland *et al*, 2010; Magrane *et al*, 2014; Lin *et al*, 2017; Moller *et al*, 2017).

To clarify proteasome-mediated stress-resilient responses in damaged motor neurons, we developed a unique mouse system in which mitochondria are labeled with GFP (as a physiological indicator) and the proteasome is specifically ablated in nerve-injured motor neurons. In addition, we established ALS mice wherein mitochondria are selectively labeled in stress-responsive motor neurons at a pre-symptomatic stage without injury. To ensure responsiveness to damage, we employed the activating transcription factor (*Atf3*) gene as a regulatory element. ATF3 is robustly induced in injured neurons to elicit transcriptional reprogramming (Nakagomi *et al*, 2003; Seijffers *et al*, 2006; Chandran *et al*, 2016; Palmisano *et al*, 2019; Lu *et al*, 2020; Renthal *et al*, 2020). Intriguingly, ATF3 is also expressed in a specific subtype of motor neurons vulnerable to degeneration in an ALS mouse model (Vlug *et al*, 2005; Saxena *et al*, 2009; Morisaki *et al*, 2016).

Using the newly established mouse system, we identified ankyrin G (AnkG) as a crucial target of the proteasome in damaged motor neurons. AnkG acts as an organizer of the axon initial segment (AIS) by recruiting and assembling submembrane proteins, such as voltage-gated sodium channels and neurofascin-186 (Huang & Rasband, 2018; Leterrier, 2018). The AIS is a transition compartment between the soma and axon that functions as a selective filter for axonal vesicles in addition to generating action potentials. Traumatic injuries dismantle the AIS, while pathogenic conditions such as tau mutation can impair AIS plasticity, leading to hyperexcitability (Schafer *et al*, 2009; Marin *et al*, 2016; Sohn *et al*, 2019). The cysteine protease calpain is considered to be responsible for degradation of the AIS (Schafer *et al*, 2009; Zhao *et al*, 2020), although alternative degradation systems may also contribute to this event (Hamdan *et al*, 2020). The physiological significance and exact mechanisms of AIS morphological changes during brain damage and disease have not been well addressed.

Here, we demonstrate a new proteasome-mediated mechanism *in vivo*, in which damaged motor neurons temporarily dismantle the

AIS in a proteasome-sensitive manner. Transient disassembly of the AIS facilitates mitochondrial entry into damaged axons. This regulatory mechanism of mitochondrial logistics may be a critical post-translational stress response that permits damaged motor neurons to produce enough energy for their regeneration or preservation of axon integrity.

Results

Mouse model of proteasome impairment specifically in nerve-injured motor neurons

We used a hypoglossal motor nerve injury as a simple and elegant experimental model for motor neuron damage (Fig 1A). It has many experimental advantages; clear onset of damage, convenience of histological and biochemical comparison between control and injured motor neurons because hypoglossal motor neurons are densely located in bilateral neighboring hypoglossal nuclei, the regenerative ability of injured motor neurons, and numerous shared stress responses with ALS motor neurons (Nakagomi *et al*, 2003; Kiryu-Seo *et al*, 2005, 2006; Lobsiger *et al*, 2007; Saxena *et al*, 2009; Sun *et al*, 2015; Maor-Nof *et al*, 2021).

To generate mouse wherein proteasome ablation occurs specifically in injured motor neurons, we used *Atf3*:BAC2 Tg mouse as a Cre driver mouse (Fig 1B). *Atf3*:BAC2 Tg mouse was designed to simultaneously express mitochondria-targeted green fluorescent protein (GFP) and Cre recombinase in an injury-specific manner, as driven by the *Atf3* gene element within a bacterial artificial chromosome (BAC); multiple previous studies, including ours, have used ATF3 as a marker for nerve injury (Nakagomi *et al*, 2003; Seijffers *et al*, 2006; Kiryu-Seo *et al*, 2008). The initiation codon of *Atf3* gene in BAC was replaced by that of GFP with the mitochondrial targeting sequence, so that *Atf3*:BAC2 Tg mice did not express exogenous ATF3. The *Atf3*:BAC2 Tg mouse is a different line from the *Atf3*:BAC Tg mouse we previously reported (Kiryu-Seo *et al*, 2016). Thus, we first examined that *Atf3*:BAC2 Tg mice began to express

Figure 1. Injury-induced *Rpt3* CKO mice decrease the mitochondrial number in injured motor axons.

- A Schematic diagram of hypoglossal nerve injury model. The axons of motor neurons in hypoglossal nucleus (XII) are projected to tongue muscle. Unilateral hypoglossal nerve is transected. Red box indicates the peripheral part of injured nerve observed in (F) and (G).
- B Schematic diagram for injury-induced deletion of proteasome subunit, *Rpt3*, from motor neurons. *Atf3*:BAC2 transgene and floxed *Rpt3* gene are presented. The initiation codon of *Atf3* in BAC is replaced by that of Mito-AcGFP. Black and white boxes indicate coding and non-coding regions of exon, respectively. Arrowheads denote loxP sites. *Rpt3* deletion and mitochondrial labeling occur at the same time in injured motor neurons. See Fig EV1D–G and Materials and Methods for details.
- C The immunostaining of GFP and RPT3 protein in hypoglossal nucleus (XII) of *Atf3*:BAC2 Tg and *Rpt3* CKO mice at 5 days (5d) after axotomy. Arrows show *Rpt3*-deleted injured motor neurons. cc, central canal.
- D 3D images of GFP-labeled mitochondria (mtGFP) in the transparent brainstem of *Atf3*:BAC2 Tg and *Rpt3* CKO mice at 5 days after hypoglossal nerve injury. Inset shows the direction and portion observed by light sheet microscopy. White arrows indicate the magnified area shown in (E). (D, C, and L) indicate dorsal, caudal, and lateral directions, respectively.
- E The magnified injured axons labeled by mtGFP.
- F Whole-mount visualization of mitochondria in injured hypoglossal motor axon at 5 days after injury.
- G Immunostaining of injured hypoglossal nerves for GFP and cytochrome c (Cytc) at 5 days after injury.
- H Number of mitochondria in injured axons of *Atf3*:BAC2 Tg and *Rpt3* CKO mice at 5 days after injury ($n = 5$ mice per group).
- I Total number of GFP-positive injured motor neurons in *Atf3*:BAC2 Tg and *Rpt3* CKO mice at 5 days after injury ($n = 4$ mice per group).
- J Number of GFP-positive mitochondria in soma at 5 days after injury. Data are shown as the mean \pm s.e.m. ($n = 3$ mice). See also Fig EV2G and H.

Data information: Data are shown as the mean \pm s.e.m., ** $P = 0.0005$ in (H), no significant difference ($P = 0.8915$) in (I) and * $P = 0.0068$ in (J), determined by unpaired t -test. Dashed lines reveal hypoglossal nucleus in (C), midline of the brain in (D) and axon in (F and G). Scale bars, 150 μ m in (C, top) and 20 μ m in (C, middle and bottom), 500 μ m in (D), 50 μ m in (E), 5 μ m in (F), and 2.5 μ m in (G).

Source data are available online for this figure.

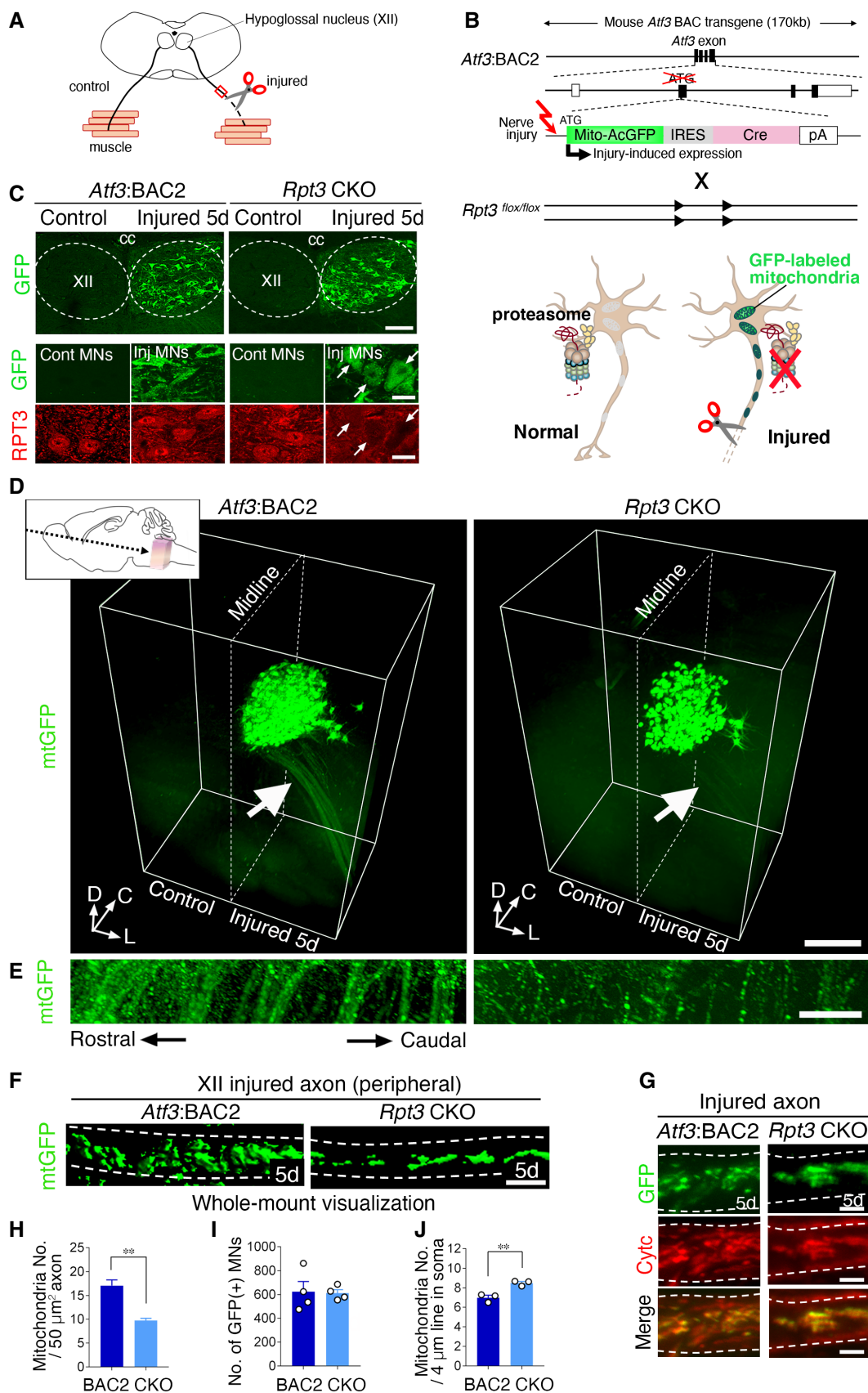


Figure 1.

GFP in injured motor neurons at 20 h after injury and thereafter increased the number of GFP-positive cells. In total, 60–70% of ATF3-positive motor neurons expressed GFP following nerve injury (Fig EV1A–C).

By crossing *Atf3*:BAC2 Tg mouse with mouse floxed for *Rpt3*, an essential subunit of 26S proteasome for the protein degradation, we generated injury-induced proteasome-deficient mouse (*Rpt3* CKO) (Figs 1B and EV1D–G). Injury-induced *Rpt3*-deficient mouse is a uniquely advantageous experimental tool to examine proteasome-mediated early stress responses in damaged motor neurons. *Rpt3* CKO mice reached adulthood, whereas the previously reported *Rpt3* knockout mouse died during early gestation (Sakao et al, 2000). We used *Atf3*:BAC2 Tg mice instead of *Atf3*:BAC Tg mice in this study, because the progeny of *Rpt3* CKO mice crossed with *Atf3*:BAC Tg mice had a shorter life span. *Atf3*:BAC2 Tg mice and *Rpt3* CKO mice exhibited identical numbers of choline acetyltransferase (ChAT)-positive hypoglossal motor neurons under the normal condition (Appendix Fig S1A and B). The expression of endogenous RPT3 protein was specifically abolished in GFP-positive injured motor neurons of *Rpt3* CKO mice by 5 days after injury, whereas RPT3 protein expression was maintained in control motor neurons of *Rpt3* CKO mice and both control and injured motor neurons of *Atf3*:BAC2 Tg mice (Fig 1C).

Injury-induced *Rpt3*-ablated motor neurons decrease numbers of mitochondria in axons

To clarify the cellular responses affected by proteasome deficiency, we acquired three-dimensional (3D) images of the transparent brains of *Atf3*:BAC2 Tg and *Rpt3* CKO mice at 5 days after hypoglossal nerve injury, because these mice enabled us to observe GFP-labeled mitochondria in nerve-injured motor neurons, which are a good indicator of the cellular status (Fig 1D). Day 3–7 is the time point when dramatic change in protein expression occurs after injury. Three-dimensional images acquired by lightsheet microscopy clearly demonstrated global views of injured hypoglossal motor neuron morphologies in mice (Fig 1D; Movies EV1 and EV2). We found that the intensity of GFP signal was reduced throughout injured motor axons of *Rpt3* CKO mice (Fig 1D and E). 3D images provided

us the useful information, which ordinary histological sections missed. We further observed whole-mount peripheral injured axons of both *Atf3*:BAC2 Tg and *Rpt3* CKO mice using a confocal microscopy with higher-resolution, to count numbers of mitochondria in injured axons more precisely (Figs 1F and EV2). The number of mitochondria in injured axons of *Rpt3* CKO mice was significantly reduced compared with *Atf3*:BAC2 Tg mice (Fig 1H). Notably, this result was not due to unlabeled mitochondria in *Rpt3* CKO mice because the results shown in Fig 1G confirmed that staining of cytochrome c (a mitochondrial marker) in injured axons of both mice was completely consistent with GFP-labeled mitochondria. When we examined lysosomes as one of the other cargos in injured axons, the distribution was not affected by *Rpt3* deletion at least 5 days after injury (Fig EV2B–D), suggesting that mitochondria and lysosomes move separately by different mechanisms in response to damage. Thereafter, lysosomes in *Rpt3*-deficient injured axons were significantly increased at 10 days after injury, probably reflecting the impairment of axonal transport or endolysosomal-autophagic systems in severely degenerating axons. The total number of GFP-positive injured motor neurons was similar in *Atf3*:BAC2 Tg and *Rpt3* CKO mice (Figs 1I and EV2E and F). Super-resolution microscopy further showed that mitochondrial density within soma of injured motor neurons seemed to be higher in *Rpt3* CKO mice (Figs 1J and EV2G and H). Thus, our findings indicate the possibility that proteasome deficiency affects mitochondrial dynamics in injured axons at early time points after injury.

Injury-induced *Rpt3*-ablated motor neurons exhibit ALS-relevant degeneration, despite their regenerative potential

To further examine the cellular condition at 5 days after axotomy, we performed quantitative reverse-transcription PCR (qRT-PCR) for the expression of regeneration-associated genes (RAGs) using control and injured hypoglossal nuclei. Unexpectedly, the alteration of mRNA expression of RAGs after injury did not show any significant difference between *Atf3*:BAC2 Tg and *Rpt3* CKO mice (Fig 2A). In addition, the expression patterns of representative regeneration-associated proteins, which were up- and downregulated, were similar in injured motor neurons of *Atf3*:BAC2 Tg mice and *Rpt3* CKO

Figure 2. Injury-induced *Rpt3*-ablated motor neurons show regenerative responses but degenerate.

- The fold change in the mRNA expression of regeneration-associated genes (RAGs) in injured hypoglossal nuclei compared with control hypoglossal nuclei of *Atf3*:BAC2 Tg and *Rpt3* CKO mice at 5 days following nerve injury. Data are shown as the mean \pm s.e.m. Fold changes in RAGs before and after injury have no significance between *Atf3*:BAC2 Tg and *Rpt3* CKO mice, determined by unpaired *t*-test (3 independent experiments).
- The expression of representative regeneration-associated proteins is properly up- or downregulated in injured motor neurons of *Rpt3* CKO mice at 5 days following hypoglossal nerve injury.
- Thionine-stained motor neurons of *Atf3*:BAC2 Tg and *Rpt3* CKO mice at 7, 14, and 17 days after hypoglossal nerve axotomy. Arrows indicate the loss of motor neurons.
- The graph showing the percentage of surviving motor neurons on the injured side compared with that on the control side. Data are shown as the mean \pm s.e.m. (***P* = 0.0002, ****P* < 0.0001, determined by unpaired *t*-test, *n* = 5 mice per group at each time point).
- The P62- and TDP-43 positive immunostaining in control and injured motor neurons (MNs) of *Atf3*:BAC2 Tg and *Rpt3* CKO mice at 7 days after hypoglossal nerve axotomy. Arrowheads show injured MNs with the accumulated proteins.
- Regenerating axons and neuromuscular junction (NMJ) in tongue of *Atf3*:BAC2 Tg and *Rpt3* CKO mice. Arrowheads show GFP-labeled mitochondria in regenerating motor axons to reform NMJ. The boxed region is magnified in inset, showing GFP-labeled mitochondria, axon (Tuj1) and α -Bungarotoxin (BTX).
- Immunostaining of ChAT and GFP-positive motor neurons of *Atf3*:BAC2 Tg mouse at 28 days after hypoglossal nerve injury.

Data information: Dashed lines outline hypoglossal nucleus in (B, C, and G). Xll, hypoglossal nucleus; cc, central canal. Scale bars, 150 μ m in (B and C), 100 μ m in (G), 20 μ m in (E and F), 10 μ m in (F inset), and 5 μ m in (E inset).

Source data are available online for this figure.

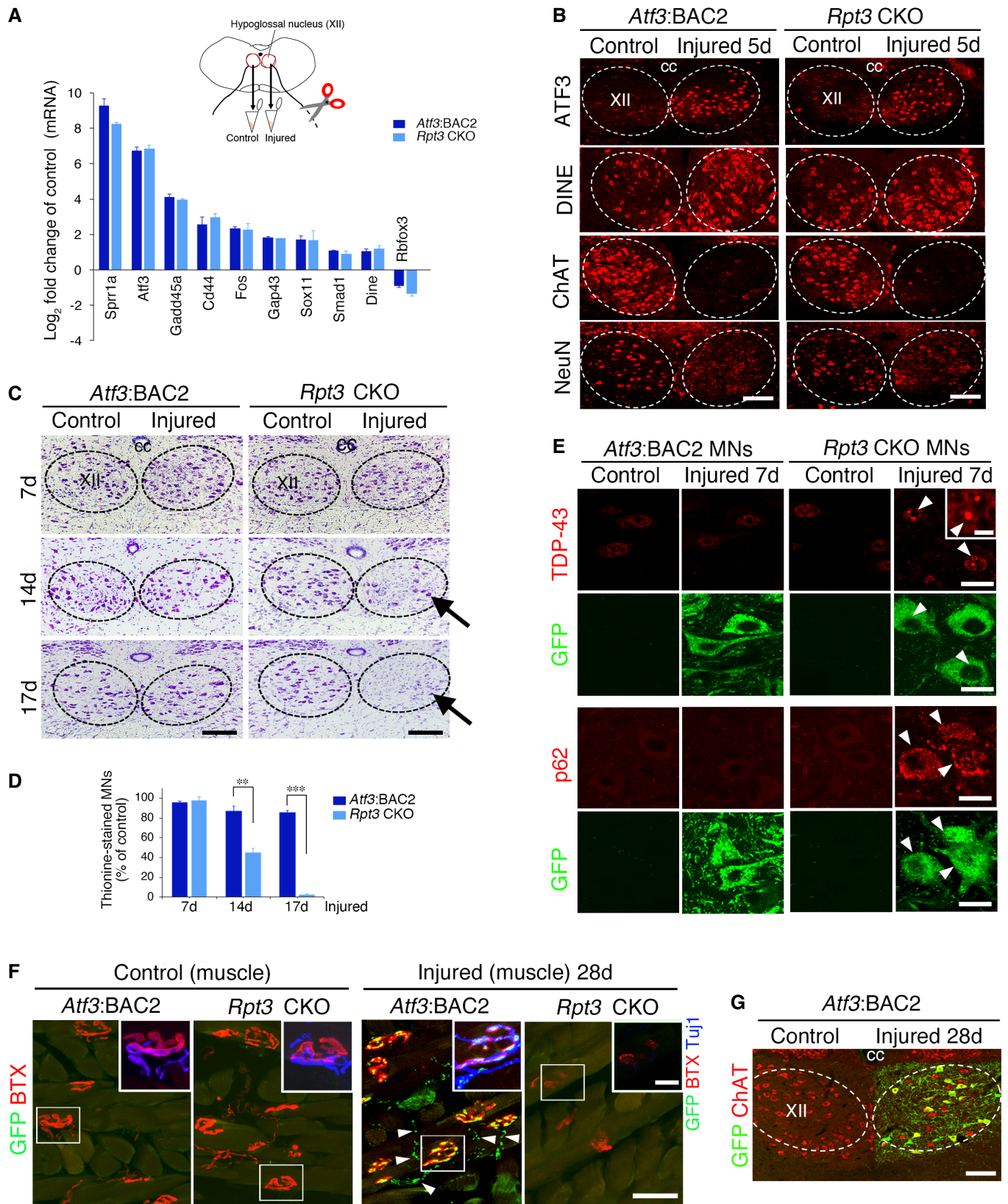


Figure 2.

mice at 5 days after injury (Fig 2B). Downregulation of ChAT and NeuN proteins in *Rpt3*-deficient injured motor neurons is probably due to compensatory autophagy system. We next examined the fate of motor neurons after hypoglossal nerve injury. Thionine staining showed that motor neurons of *Rpt3* CKO mice survived at 7 days after injury, similar to those of *Atf3*:BAC2 Tg mice; thereafter, those in *Rpt3* CKO mice began to degenerate and died completely by 17 days after injury, while around 85% of injured motor neurons of *Atf3*:BAC2 Tg survived (Fig 2C and D). Microglial hyper-activation but not astrocyte was also observed at the proximity of the *Rpt3*-deleted injured motor neurons at 7 days after injury (Appendix Fig S1C and D). These results suggest that proteasome-mediated stress pathways are located at a critical point for further regeneration to proceed after regenerative programming. *Rpt3*-deleted injured motor neurons accumulated TDP-43 and p62 around 7 days after injury (Fig 2E). The accumulation of TDP-43 was shown in nucleus in our study, although it was generally exported and accumulated in the cytoplasm in ALS motor neurons. Its accumulation in nucleus may be a stress response rather than pathology, as previously described (Udan-Johns *et al*, 2014). Aggregation of p62, an autophagic marker, could indicate the compensation for proteasome impairment in injured motor neurons of *Rpt3* CKO mice, although the ubiquitin-proteasome system (UPS) is a dominant protein degradation system in motor neurons (Tashiro *et al*, 2012). The injured axons of *Atf3*:BAC2 Tg mice, in which GFP-labeled mitochondria were transported from soma upon injury, reinnervated the muscle in tongue and initiated to reform neuromuscular junctions (NMJs) at 28 days after injury, while those of *Rpt3* CKO mice did not (Fig 2F). Injured motor neurons in *Atf3*:BAC2 Tg mice also survived at 28 days after injury (Fig 2G). Collectively, *Rpt3*-deleted motor neurons have competence to regenerate during the initial stage of nerve injury response, but likely degenerate. Dysfunction of proteasome-mediated response during the initial stage may be involved.

Axon injury-induced disappearance of the AIS is suppressed in *Rpt3* CKO mice

Based on 3D imaging results shown in Fig 1, we considered that proteasome dysfunction might affect the entry of mitochondria from the soma to injured axons at early time points after injury, a time when motor neuron death was not apparent (Fig 2). A transition compartment between the soma and axon is known as the AIS. Previous studies have reported the AIS changes its morphology in response to neuronal activity and neuronal insults (Yamada & Kuba, 2016; Huang & Rasband, 2018). We examined morphological changes in the AIS before and after hypoglossal nerve injury using higher-resolution cellular and subcellular 2D confocal images (Fig 3A and B). Immunohistochemistry for AnkG, an organizer of the AIS, demonstrated that the AIS disappeared in injured motor neurons of *Atf3*:BAC2 Tg mice at 5 days after injury, while the AIS remained in those of *Rpt3* CKO mice (Fig 3C). As shown in Fig 3D and E, the difference of AIS number and length in injured motor neurons between *Atf3*:BAC2 Tg mice and *Rpt3* CKO mice at day 5 was statistically significant. The number and length of the AIS were then recovered in injured motor neurons of *Atf3*:BAC2 Tg mice at 28 days after nerve injury, suggesting the reassembly of the AIS structure. AIS and GFP-positive injured motor neurons were not

detected in *Rpt3* CKO mice at 28 days after injury, because the injured motor neurons degenerated as shown in Fig 2C and D and F. The number of AIS in *Atf3*:BAC2 Tg mice was not completely recovered to the control level at 28 days after injury (Fig 3D), because all of the injured motor neurons in *Atf3*:BAC2 Tg mice did not regenerate in this model. These findings suggest that temporal disassembly of the AIS in injured motor neurons is a positive stress response mediated by the proteasome.

AnkG is degraded by the ubiquitin-proteasome system

We next attempted to clarify whether AnkG can be degraded by the UPS upon injury. We performed qRT-PCR using control and injured hypoglossal nuclei of wild-type mice collected at 5 days after axotomy, to examine transcriptional regulation of AnkG before and after injury (Fig 4A). The results showed that mRNA expression of AnkG was unaltered before and after injury, while that of *Atf3* and *Chat* as positive and negative RAGs was dramatically up- and down-regulated, respectively. The longer AnkG splicing variant called giant AnkG, which is considered to be responsible for AIS formation, was also unchanged before and after injury. Thus, the regulation of AnkG at protein level is critical after nerve injury.

A computer search such as UbPred predicted that AnkG protein has multiple ubiquitination sites. To examine ubiquitination of AnkG, we performed a ubiquitination assay using cell lysates in which sequentially fragmented AnkG constructs were transfected into COS-7 cells (Fig 4B). A fragmented construct of AnkG was used for the ubiquitination assay because full-length AnkG was too long for this experiment. The results showed that most AnkG fragments were experimentally poly-ubiquitinated, suggesting that AnkG protein could be degraded by the UPS. Immunoblots of control and injured hypoglossal nuclei showed that both 480 and 270-kDa forms of AnkG were downregulated after injury, while injured nerves exhibited no signals for 480-kDa of AnkG and no obvious changes of 270-kDa and major 190-kDa AnkG between control and injured nerves (Fig 4C). A previous study reported that AnkG was degraded by the calcium-dependent protease calpain into ~95 and 72-kDa forms (Schafer *et al*, 2009). However, injured hypoglossal nuclei did not exhibit breakdown products, suggesting the possibility that proteasome is dominantly involved in this injury model. Immunohistochemical staining revealed that the broadly scattered dot-like signals of AnkG were still present in the injured side of the hypoglossal nucleus, while AnkG-positive AIS was lost in injured motor neurons of *Atf3*:BAC2 Tg mice (Fig 4D). These dot-like signals were assumed to be nodes of Ranvier (node), which exhibit similar protein components to the AIS. When we examined the nodes of hypoglossal motor nerves, both control and injured motor axons similarly exhibited signals for AnkG and Caspr, indicators of nodes and paranodes, respectively. Collectively, these results indicate that proteasome-mediated AnkG degradation occurred specifically in the AIS, but not in nodes of injured motor neurons.

Nerve injury-induced disassembly of AIS enhances mitochondrial influx into axons

We next evaluated the physiological significance of proteasome-dependent disassembly of the AIS in injured motor neurons. We

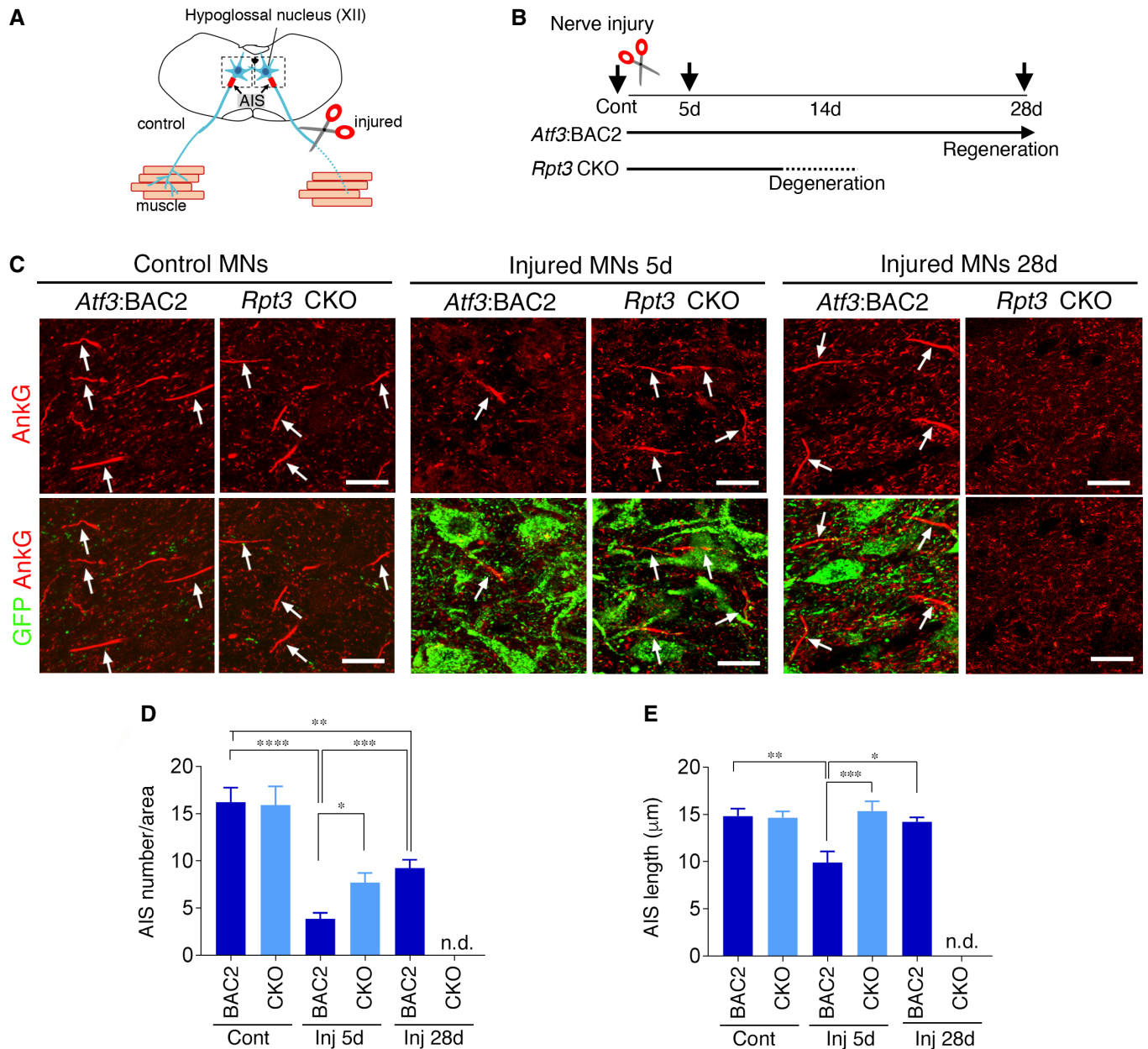


Figure 3. Injury-induced ablation of *Rpt3* affects the disassembly of the AIS in injured motor neuron.

A Schematic diagram of the AIS in hypoglossal nerve injury model.

B Schematic showing the time course of motor neurons after nerve injury. Arrows indicate the time point at which the experiments were performed.

C Hypoglossal motor neurons of *Atf3:BAC2* Tg and *Rpt3* CKO mice before and at 5 days (5d) and 28 days (28d) after injury, immunostained by AnkG and GFP. Arrows indicate the AIS stained by AnkG. Scale bars, 20 µm.

D Quantification of the number of the AIS in control (Cont) and injured (Inj) hypoglossal motor neurons of *Atf3:BAC2* and *Rpt3* CKO mice. Data are expressed as mean ± s.e.m. * $P = 0.043$, ** $P = 0.0162$, *** $P = 0.008$, **** $P < 0.0001$, determined by one-way ANOVA followed by *Tukey post hoc* analysis, n.d., not detected, $n = 5$ mice for each group.

E Quantification of the AIS length in control (Cont) and injured (Inj) hypoglossal motor neurons of *Atf3:BAC2* and *Rpt3* CKO mice. Data are expressed as mean ± s.e.m. * $P = 0.0087$, ** $P = 0.0024$, *** $P = 0.0007$, determined by one-way ANOVA followed by *Tukey post hoc* analysis, n.d., not detected, $n = 5$ mice for each group.

Source data are available online for this figure.

hypothesized that the absence of the AIS was beneficial for mitochondrial entry into injured axons. To evaluate this hypothesis, we focused on mitochondrial localization in the AIS region before and

after hypoglossal nerve injury (Fig 5A). *Atf3:BAC2* Tg mice exhibited mutually exclusive distribution of AnkG-positive AIS and mitochondria (Fig 5B). The AIS of *Atf3:BAC2* Tg mice was gradually

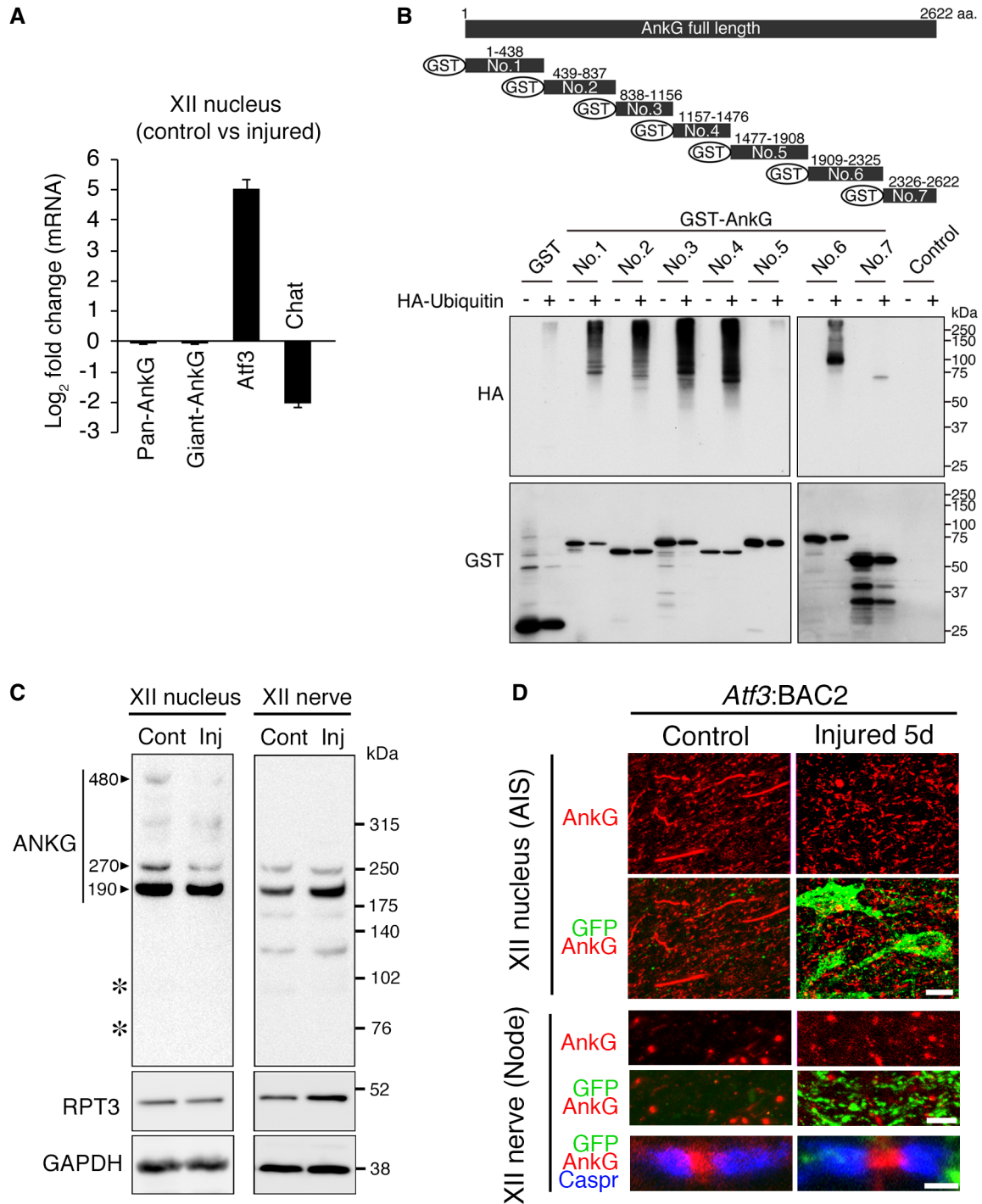


Figure 4. Proteasome is responsible for the AIS-specific degradation of AnkG in injured motor neurons.

A Graph represents fold change in mRNAs in injured hypoglossal (XII) nuclei compared with control hypoglossal nuclei of wild-type mice at 5 days after injury. Data are shown as the mean ± s.e.m. (*n* = 3 independent experiments).

B Ubiquitination assay of AnkG protein. The lysates of COS-7 cells expressing the indicated truncated AnkG tagged with GST and HA-Ubiquitin were pulled down with glutathione Sepharose beads, followed by western blotting with anti-HA and anti-GST antibodies.

C Western blot of hypoglossal nuclei (left) and nerves (right) at 5 days after injury with anti-AnkG, RPT3 and GAPDH antibodies. AnkG products of 190/270/480 kDa are indicated by arrowheads. The positions of the degraded products by calpain are shown by asterisks at ~ 95 kDa and 72 kDa.

D The expression of AnkG (red) and GFP (green) in the AIS of hypoglossal (XII) motor neurons and that of AnkG, GFP, and Caspr (blue) in nodes of hypoglossal motor nerves at 5 days after injury. Scale bars, 15, 5, and 1.5 μm from the top.

Source data are available online for this figure.

disassembled in response to injury and subsequently reassembled at 28 days after injury along with regeneration. In contrast, numerous GFP-labeled mitochondria appeared in the AnkG-disappeared region of the AIS after injury, while a limited number of mitochondria remained in the recovered AIS region at 28 days after injury. This was not an artificial effect of *Atf3*:BAC2 Tg mice because the widely described *Thy1*-Mito mouse, in which mitochondria are labeled by CFP in neurons under control of the *Thy1* promoter, showed a similar relationship between the AIS and mitochondria (Fig EV3A–E). Unlike injured motor neurons in *Atf3*:BAC2 Tg mice, *Rpt3*-deficient injured motor neurons preserved the AIS at 5 days after injury and exhibited few GFP-labeled mitochondria in it (Fig 5C–E). Correlatively, the number of mitochondria in axotomized motor nerves of *Atf3*:BAC2 Tg mice was significantly increased compared with normal nerves of *Thy1*-Mito mice and subsequently returned to a control level along with the AIS recovery (Fig 5F and G). However, numbers of mitochondria in *Rpt3*-deficient nerves did not show any injury-induced changes, suggesting that the presence or absence of the AIS is involved in regulating mitochondrial influx into injured axons.

To further address whether the loss of the AIS is directly involved in the increased number of mitochondria observed in injured axons or whether the two events are independent, we forced disruption of the preserved AIS structures in injured motor neurons of *Rpt3* CKO mice. An AnkG shRNA was designed to suppress the larger splicing variant of AnkG. After injecting an AAV carrying AnkG shRNA into the tongue, it was retrogradely transported into motor neurons, whereby it suppressed AnkG expression (Figs 5H and EV4A and B). Our results showed that infection with AAV-AnkG shRNA disrupted the AIS, and numbers of GFP-labeled mitochondria in *Rpt3*-ablated injured motor neurons were increased (Fig 5I–K). Infection with AAV-scramble shRNA affected neither the appearance of the AIS nor the localization of GFP-labeled mitochondria in *Rpt3*-deficient injured motor neurons. Infection with AAV-AnkG shRNA in uninjured

motor neurons of *Thy1*-Mito mouse did not increase the number of GFP-labeled mitochondria in axons, suggesting that injury-induced driving forces are necessary to increase mitochondrial density in axons (Fig EV4C and D). Furthermore, we examined whether the knockdown of AnkG influences the survival of *Rpt3*-deficient injured motor neurons or not. The infection of AAV-AnkG shRNA delayed the death of *Rpt3*-deficient injured motor neurons, compared with that of AAV-scramble shRNA (Fig 5L and M). These results suggest that the AIS disassembly is necessary for injury-induced increase in mitochondrial influx into the axons to promote regeneration.

Mitochondrial motility in injured axons is reduced in *Rpt3* CKO mice

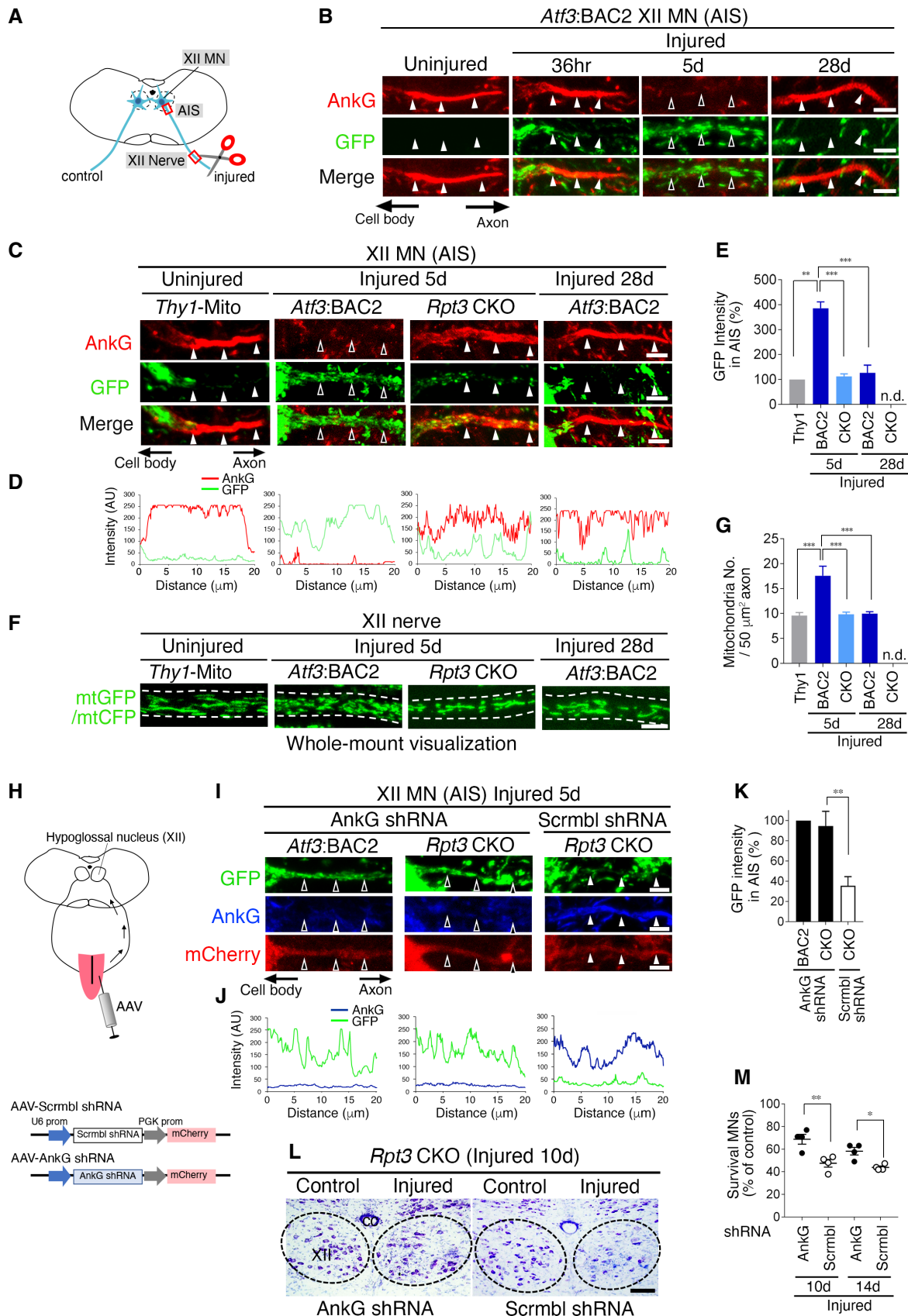
Because two types of mitochondria, motile and stationary, are present in axons, we examined which type was responsible for the observed change in mitochondrial numbers in injured axons. For live imaging of mitochondrial flow, we used another nerve injury model: sciatic nerve injury (Fig 6A). Injured motor neurons after sciatic nerve injury showed similar responses of the AIS and mitochondria to those of hypoglossal nerve injury (Fig EV3C–E; Appendix Fig S2A and B). We performed live imaging of CFP- or GFP-labeled mitochondria in uninjured sciatic nerves of *Thy1*-Mito mice and injured sciatic nerves of both *Atf3*:BAC2 Tg mice and *Rpt3* CKO mice (Fig 6B and C). *Atf3*:BAC2 Tg mice exhibited increased numbers of motile mitochondria in injured nerves compared with *Thy1*-Mito mice and *Rpt3* CKO mice (Fig 6D and E). Increased numbers of motile mitochondria in injured sciatic nerves of *Atf3*:BAC2 Tg mice returned to control levels along with regeneration. Notably, stationary mitochondria were not significantly altered in any of these mice (Fig 6F). Nerve injury induces proteasome-dependent AIS degradation in motor neurons, which could be coupled with the increase in mitochondrial transport into axons under the presence of driving forces.

Figure 5. Absence of the AIS facilitates mitochondrial influx to injured axons.

- Schematic diagram of hypoglossal nerve injury model. The areas shown by the red boxes (the AIS and hypoglossal (XII) nerve) are observed in this fig.
- Time-dependent localization of AnkG and GFP-labeled mitochondria in motor neuron (MN) of *Atf3*:BAC2 Tg mouse before and after hypoglossal nerve injury.
- The localization of AnkG and GFP-labeled mitochondria in the AIS of uninjured MN of *Thy1*-Mito Tg mice and injured motor neurons of *Atf3*:BAC2 Tg and *Rpt3* CKO mice.
- Graphs show the GFP and AnkG fluorescent intensity scans corresponding to (C) over a 20 μ m line running from the soma to the axon.
- Graph represents the percentage (%) of GFP intensity in the AIS, compared with that in the AIS of *Thy1*-Mito mouse ($n = 5$ mice per group).
- Whole-mount observation of GFP- or CFP-labeled mitochondria (mtGFP or mtCFP) in the proximal region of peripheral hypoglossal (XII) nerve as shown in (A). Dashed lines outline the axon.
- Graph shows mitochondrial number in hypoglossal (XII) axon ($n = 5$ mice).
- Schematic diagram demonstrating the AAV infection to tongue and the AAV constructs.
- Altered localization of the GFP-labeled mitochondria in the AIS of injured motor neurons of AnkG shRNA AAV-infected *Rpt3* CKO mice at 5 days after injury.
- Fluorescent intensity scans of GFP and AnkG corresponding to (I).
- Graph represents the percentage (%) of GFP intensity in the AIS, compared with that in the AIS of *Atf3*:BAC2 Tg mouse treated with AnkG shRNA ($n = 5$ mice per group).
- Thionine-stained hypoglossal motor neurons of *Rpt3* CKO mice at 10 days after injury. *Rpt3* CKO mice are infected by AnkG shRNA or scramble shRNA AAVs. Dashed lines outline hypoglossal nucleus. XII, hypoglossal nucleus; cc, central canal.
- The percentage of surviving motor neurons on the injured side compared with that on the control side in *Rpt3* CKO mice after infection of AnkG shRNA or scramble shRNA AAVs ($n = 4$ mice per group).

Data information: For (E, G, K, and M), data are shown as the mean \pm s.e.m., $^{**}P = 0.0003$, $^{***}P < 0.0001$ in (E and G), $^{**}P = 0.0064$ in (K), $^{*}P = 0.0405$, $^{**}P = 0.003$ in (M), determined by one-way ANOVA followed by *Tukey post hoc* test, n.d., not detected. In (B, C, and I), closed arrowheads denote the presence of the AIS, while open arrowheads show disappeared AIS. Scale bars, 5 μ m in (B, C, F, and I) and 100 μ m in (L).

Source data are available online for this figure.



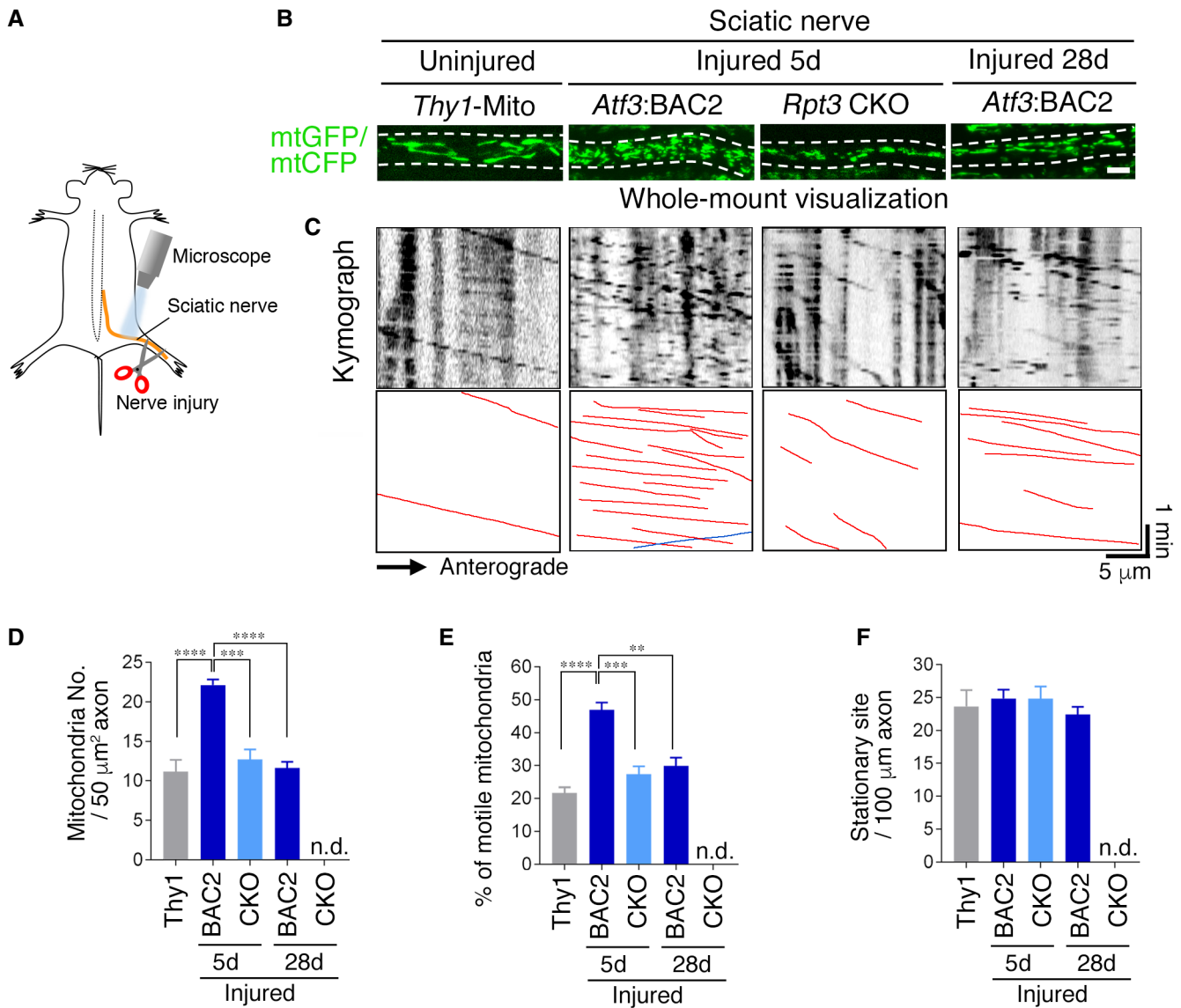


Figure 6. Mitochondrial motility in injured axons is up-regulated in *Atf3*:BAC2 Tg mice but not in *Rpt3* CKO mice.

A Schematic diagram demonstrating live imaging of sciatic nerve.

B Whole-mount visualization of GFP- or CFP-labeled mitochondria (mtGFP or mtCFP) in sciatic nerve. Dashed lines indicate the boundary of axon. Scale bar, 5 μm .

C Representative kymographs showing the behavior of mtCFP in uninjured sciatic nerves of *Thy1*-Mito Tg and mtGFP in injured sciatic nerves of *Atf3*:BAC2 and *Rpt3* CKO mice.

D–F The number of mitochondria (D), percentage of motile mitochondria (E), and stationary mitochondrial site (F) in axons.

Data information: Data are shown as the mean \pm s.e.m. *** P = 0.0001, **** P < 0.0001 in (D), ** P = 0.0006, *** P = 0.0001, **** P < 0.0001 in (E), determined by one-way ANOVA followed by *Tukey post hoc* test, n.d., not detected, n = 5 mice for each group.

Source data are available online for this figure.

Failure of AIS disassembly in ATF3-expressing ALS motor neurons at a pre-symptomatic stage

ATF3-expressing spinal motor neurons exist in ALS mice without injury (Vlug et al, 2005; Saxena et al, 2009; Morisaki et al, 2016). We crossed *Atf3*:BAC Tg mice with *SOD1*^{G93A} (*SOD1*) ALS mice and generated *Atf3*:BAC;*SOD1*^{G93A} (*Atf3*:*SOD1*) mice to selectively label ATF3-expressing motor neurons (Figs 7A and EV5A). We used *Atf3*:

BAC Tg mice here, because *Atf3*:BAC Tg mice mimic the expression pattern of endogenous ATF3 more effectively than *Atf3*:BAC2 Tg mice. *Atf3*:*SOD1* mice showed similar life span and age-dependent motor neuron death with *SOD1* mice, suggesting that the *Atf3*:BAC transgene does not affect the disease phenotype of *SOD1* mice (Fig EV5B–D). 3D image of transparent spinal cord in *Atf3*:*SOD1* mouse clearly showed GFP-labeled motor neurons, while that of *Atf3*:BAC Tg mouse (littermate control) did not (Fig 7B;

Movie EV3). The expression of GFP was co-localized well with that of ATF3 in motor neurons of *Atf3*;SOD1 mouse (Fig 7C). Of ChAT-positive spinal motor neurons, GFP-expressing motor neurons were < 20% at P70 (pre-symptomatic stage; Fig 7D). These GFP-positive motor neurons appeared around P60, increased in number, and then degenerated along with age in *Atf3*;SOD1 mouse (Fig EV5E and F). Among the heterogeneous spinal motor neuron pool, most of GFP-positive motor neurons in *Atf3*;SOD1 mice expressed ATF3 (Fig 7E). They also expressed matrix metalloproteinase-9 (MMP-9) or osteopontin (OPN), which are reportedly localized in vulnerable motor neurons (Figs 7E and EV5G) (Kaplan *et al*, 2014; Morisaki *et al*, 2016), suggesting that stress-responsive vulnerable motor neurons are selectively labeled by GFP in *Atf3*;SOD1 mice.

Given that ALS motor neurons reduce proteasome activity (Jenkins *et al*, 2020) and initiate to induce ATF3 at pre-symptomatic stage, we wondered whether the failure of AIS disassembly in injured motor neurons of *Rpt3* CKO mice may occur in GFP-positive ALS motor neurons. We found that GFP-positive spinal motor neurons in *Atf3*;SOD1 mice retained the AIS and that the length of the AIS did not show any significant difference with that in the ChAT-positive spinal motor neurons in *Atf3*:BAC and SOD1 mice (Fig 7F and G). We next evaluated mitochondrial localization in the AIS region. Both traumatically damaged GFP-positive motor neurons in *Atf3*:BAC and pathologically damaged GFP-positive motor neurons in *Atf3*;SOD1 induce ATF3. However, pathologically damaged motor neurons failed to dismantle the AIS and exhibited few GFP-labeled mitochondria in it (Fig 7H–J). Concomitantly, GFP-positive motor neurons of *Atf3*;SOD1 mice did not increase the number of axonal mitochondria despite inducing ATF3. (Fig 7K and L).

We further confirmed that ATF3-inducing ALS motor neurons failed to disassemble the AIS using hypoglossal nerve injury model (Appendix Fig S3). The number of GFP-positive motor neurons of *Atf3*;SOD1 mice was originally much lower in the hypoglossal nucleus than in the spinal cord, probably because cranial motor neurons retained higher proteasomal activity than spinal motor neurons (An *et al*, 2019; Appendix Fig S3A–C). Almost all hypoglossal motor neurons in *Atf3*;SOD1 mice were labeled by GFP following

nerve injury because of ATF3 induction. However, they did not disassemble the AIS nor increase mitochondria (Appendix Fig S3D and E). Collectively, the ATF3-positive ALS motor neurons lack or reduce proteasome-mediated stress responses, resembling injury-induced *Rpt3*-deficient motor neurons.

Discussion

In this study, the combination of motor nerve injury model with unique genetically engineered mice has clarified a new proteasome-mediated stress-resilient mechanism that is lacking in damaged motor neurons prior to degeneration. Injury-induced *Rpt3*-deficient motor neurons fail to activate proteasome-dependent AIS disassembly and exhibit ALS-relevant degeneration, despite remaining regenerative capacity. The functional consequence of the transient AIS disassembly after neuron damage has become clear in this study. Upon damage, proteasome-mediated disruption of the AIS facilitates mitochondrial entry into axons, perhaps to compensate for the increased energy expenditure associated with axon regeneration. Intriguingly, the failure of this proteasome-mediated mechanism against pathological damage might be associated with the vulnerability of ALS motor neurons (Fig 8).

Transient AIS disassembly is critical for injured motor neurons to accelerate mitochondrial influx into axons

Here, we defined that the presence or absence of the AIS alters mitochondrial density in injured axons. It has been established that mitochondrial supply is critical for injured axons and growth cones to acquire energy for reconstruction (Chamberlain & Sheng, 2019). However, the mechanism underlying enhanced mitochondrial transport has remained elusive. Furthermore, the physiological significance of AIS dismantling in injury and disease has been unclear, although AIS plasticity has been implicated in changes in neuronal excitability. This study is the first to examine the association between damage-induced disruption of the AIS and mitochondrial

Figure 7. Failure of the AIS disassembly and mitochondrial influx in stress-responsive GFP motor neurons of *Atf3*;SOD1 mouse.

- A Breeding schemes to obtain *Atf3*:BAC; SOD1^{G93A} (*Atf3*;SOD1) mouse.
- B 3D images of GFP-labeled mitochondria (mtGFP) in the transparent spinal cord without injury of *Atf3*;SOD1 mouse at pre-symptomatic stage (P70, 70-day-old) and *Atf3*:BAC Tg mouse (inset). V, C, and L indicate ventral, caudal, and lateral directions, respectively.
- C Immunostaining of spinal cord in *Atf3*:BAC Tg and *Atf3*;SOD1 mice at P70. The boxed regions are magnified in lower panels. Arrows indicate GFP- and ATF3-positive motor neurons (MNs). Dashed lines outline the edge of the gray matter in spinal cord.
- D The percentage (%) of GFP-positive MNs (black bar) in ChAT-positive MNs of *Atf3*:BAC and *Atf3*;SOD1 mice at P70 ($n = 5$ mice per each group).
- E The percentage (%) of ATF3, MMP-9 or osteopontin (OPN)-positive MNs (black bar) in GFP-positive MNs of *Atf3*;SOD1 mice at P65–70 ($n = 5–7$ mice per group).
- F Immunostaining of AnkG in ChAT-positive spinal MN of *Atf3*:BAC and SOD1 and in GFP-positive spinal MN of *Atf3*;SOD1 mouse at P70.
- G Quantification of the AIS length ($n = 5$ mice per group).
- H The localization of AnkG and GFP-labeled mitochondria in uninjured spinal MN of *Thy1*-Mito (without ATF3 induction), traumatically sciatic nerve-injured MN of *Atf3*:BAC (with ATF3 induction) and pathologically damaged MN of *Atf3*;SOD1 mice (with ATF3 induction). Closed arrowheads denote the presence of the AIS, while open arrowheads show disappeared AIS.
- I Fluorescent intensity scan of GFP and AnkG in corresponding to (H).
- J The percentage (%) of GFP intensity in the AIS, compared with that in the AIS of uninjured MNs in *Thy1*-Mito mice ($n = 5$ mice per group).
- K Whole-mount observation of mtGFP or mtCFP in sciatic nerve. Dashed lines outline the axon.
- L The number of mtGFP or mtCFP in sciatic nerve ($n = 5$ mice).

Data information: For (D, E, G, J, and L), data are shown as the mean \pm s.e.m., no significant difference in (G), $**P = 0.0008$, $***P = 0.0007$ in (J), $**P = 0.0036$, $****P < 0.0001$ in (L), determined by one-way ANOVA followed by *Tukey post hoc* test, n.d., not detected. Scale bars, 700 μ m in (B), 1,000 μ m in (B; inset), 50 μ m in (C; upper panel), 20 μ m in (C; lower), 10 μ m in (F and K) and 5 μ m in (H). See also Fig EV5.

Source data are available online for this figure.

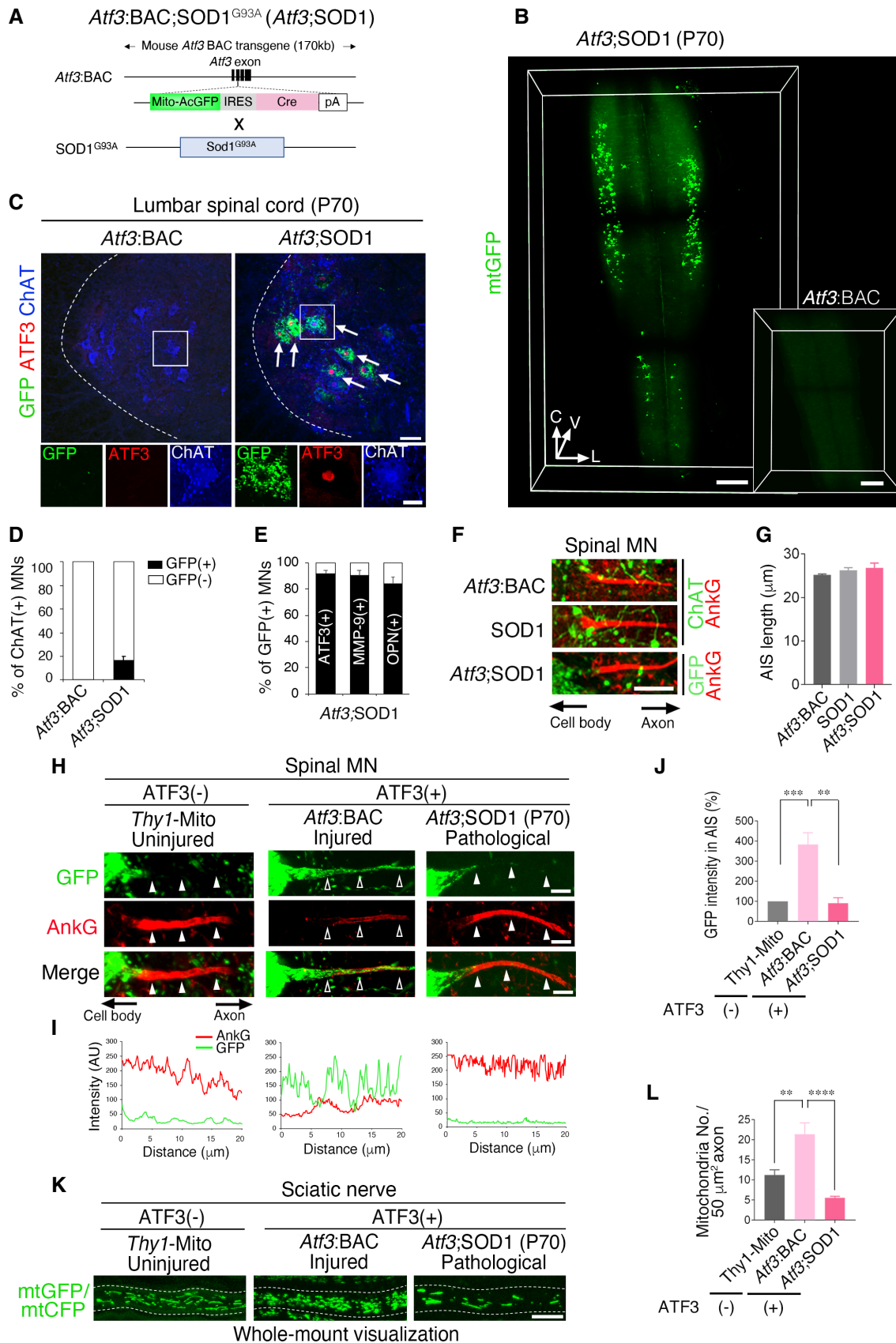


Figure 7.

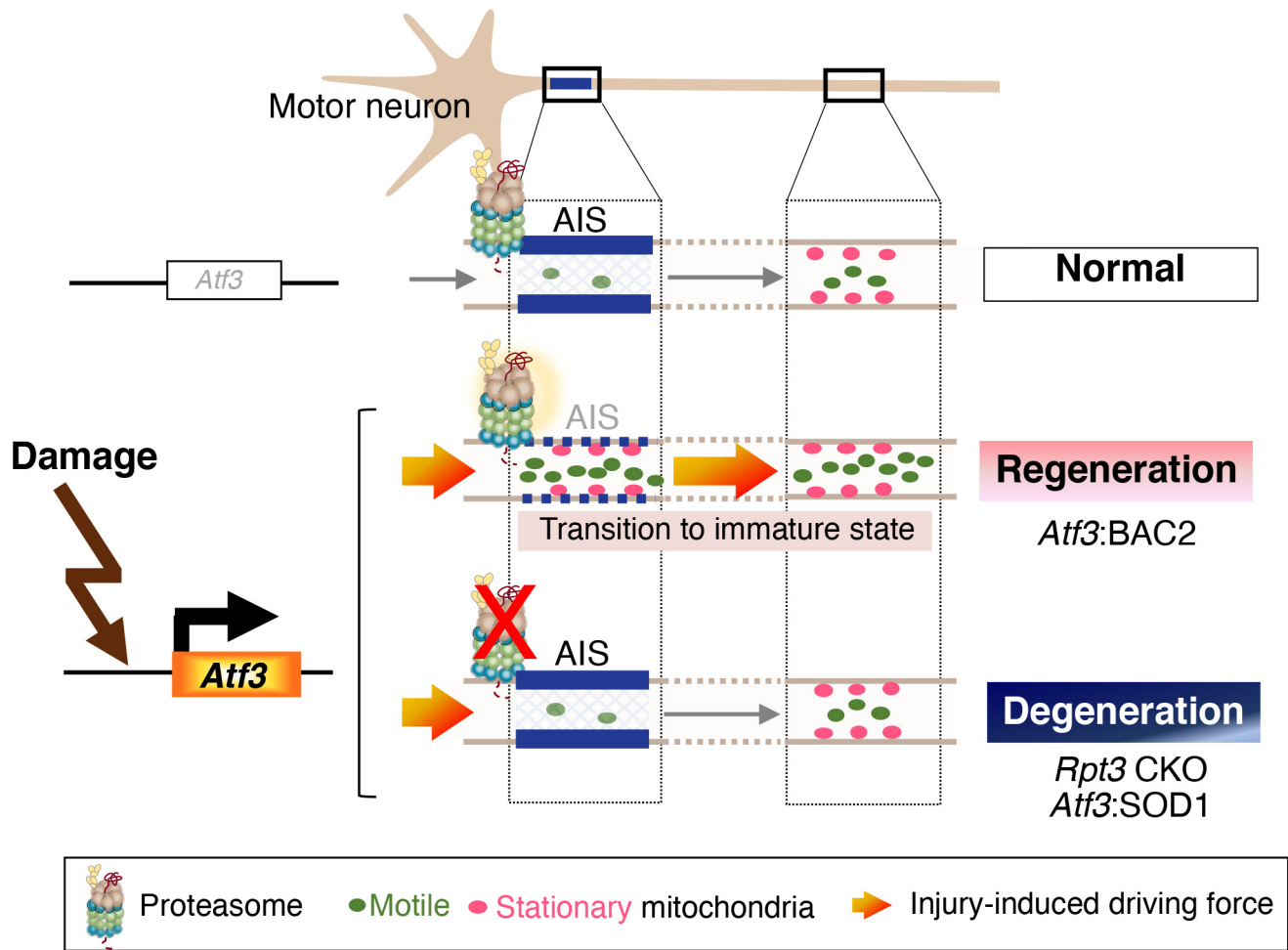


Figure 8. Schematic diagram of the proteasome-sensitive AIS disassembly and mitochondrial supply upon damage.

Damaged motor neurons induce stress-sensitive transcription factor, ATF3, to initiate regeneration program. ATF3-positive injured motor neurons temporarily dismantle the AIS in a proteasome-dependent manner and increase mitochondrial entry into injured axons under the injury-induced driving force to meet the energy demand for axon regeneration. However, proteasome-deficient injured motor neurons and stress-responsive vulnerable ALS motor neurons with proteasome dysfunction cannot activate this mechanism despite inducing ATF3.

entry *in vivo* by taking advantage of a unique mouse model. Under normal conditions, the AIS acts as a selective barrier in which nuclear distribution element-like 1 (NDEL1) excludes non-axonal cargo (Farias *et al*, 2015; Jenkins *et al*, 2015; Kuijpers *et al*, 2016; Gumy *et al*, 2017). Strikingly, suppression of AnkG does not always influence axonal transport under normal conditions, partly because the proximal axonal region contributes to selective cargo transport in addition to the AIS (Farias *et al*, 2015; Jenkins *et al*, 2015). They are consistent with our result that the suppression of AnkG did not show any obvious change in mitochondrial number in axon under normal condition. However, the situation seems to be different upon injury, whereby the activation of mitochondrial transport-associated molecules such as dual-leucine zipper kinase 1 (Dlk1), armadillo repeat-containing X-linked 1 (Armcx1), mitochondrial Rho GTPases (Miro), and dynamin-related protein 1 (Drp1) and the modification of microtubules enhance mitochondrial localization in injured axons (Hellal *et al*, 2011; Benned-Jensen *et al*, 2016; Cartoni *et al*, 2016; Kiryu-Seo *et al*, 2016; Kalinski *et al*, 2019; Han *et al*, 2020). Under

the presence of these powerful driving forces upon injury, the breakdown of the selective filter is efficient for enhanced mitochondrial entry into injured axons.

The absence of the AIS is usually observed in immature neurons. The AIS dismantling in response to injury may contribute to the temporal transition of injured motor neurons to an immature state at post-translational level, in order to acquire regenerative potential. Because immature neurons require higher mitochondrial motility in axon during development and progressively reduce it along with development (Lewis *et al*, 2016). Recent progresses have clarified that the transcriptional and epigenetic reprogramming makes injured neurons revert to immature state for regeneration (Chandran *et al*, 2016; Palmisano *et al*, 2019; Bradke *et al*, 2020; Lu *et al*, 2020; Renthal *et al*, 2020). In line with this, the proteasome-mediated disassembly of the AIS would be a post-translational mechanism after the transcriptional and epigenetic reprogramming. Injured motor neurons likely use this mechanism to meet urgent energy demand for regeneration. As we show in this study, the AIS

is reassembled at appropriate timing along with regeneration. The regulation mechanism of the AIS reassembly would also contribute to complete regeneration. Conclusively, the AIS disassembly and reassembly could be one of the key mitochondrial logistic mechanisms under emergency situations.

Proteasomal degradation is the major mechanism for AIS disassembly in damaged motor neurons

Using injury-induced *Rpt3* CKO mice, we found that AnkG, the organizing component of the AIS, could be a proteasomal target upon injury. We showed that AnkG protein was indeed poly-ubiquitinated. The data are also supported by previous study showing that 26S proteasome dysfunction in neurons caused global accumulation of ubiquitinated proteins including AnkG (Ugun-Klusek et al, 2017). We do not rule out the possibility that other protein degradation systems, such as calpain and autophagy, participate in AIS loss in injured motor neurons or play a compensatory role in *Rpt3*-deficient injured motor neurons. Most notably, calpain is considered to be responsible for degradation of the AIS after brain damage (Schafer et al, 2009; Benned-Jensen et al, 2016; Zhao et al, 2020). One possible explanation is the different dominance of protein degradation systems among neurons, because motor neurons are susceptible to proteasomal degradation rather than autophagy (Tashiro et al, 2012; Rudnick et al, 2017). Alternatively, differences in regenerative capacity between the central and peripheral nervous systems may reflect differences in degradation systems for the AIS. In central nervous system traumatic injury models, such as optic nerve injury and ischemia, both the AIS and nodes, which are composed of identical membranous proteins, seem to be disrupted (Marin et al, 2016); however, injured motor neurons in our injury model did not exhibit deteriorated nodes, perhaps because apparent demyelination did not occur. Taken together with these differences, it could be concluded that the proteasome is responsible for degradation of the AIS in damaged motor neurons. To regulate proteasome activity in an AIS-specific manner in damaged motor neurons, intrinsic or extrinsic local signaling such as signaling kinases and glial contact could be activated following injury (Yoshimura & Rasband, 2014; Baalman et al, 2015; Tamada et al, 2021). Otherwise, AIS-residing ubiquitin ligases, such as TRIM46, may participate in AIS-specific breakdown; although, thus far, TRIM46 reportedly has microtubule crosslinking activity, but not E3 ligase activity (van Beuningen et al, 2015).

Apart from disruption of the AIS, there likely exist further proteasome-mediated stress responses in injured motor neurons. Our previous study demonstrated that mitochondrial fission is a temporally adaptive response for nerve regeneration (Kiryu-Seo et al, 2016). Because mitochondrial proteins responsible for fusion/fission are regulated by degradation, the proteasome may be also involved in processes in injured motor neurons. Recently, Kong et al (2020) identified an interaction between AMPK and the proteasome in axoplasm to promote degradation and drive regeneration (Kong et al, 2020). Considering that uninjured motor neurons maintain the AIS in the presence of the proteasome, *Rpt3*-deficient uninjured motor neurons which were previously reported would degenerate in different mechanisms from the failure of the AIS disassembly (Tashiro et al, 2012). Therefore, other multiple proteasome-dependent stress responses or injury-independent proteasome

functions would also participate in resilience of damaged motor neurons.

Failure of AIS disassembly and subsequent mitochondrial insufficiency in vulnerable type of ALS motor neuron

Given that injury-induced *Rpt3*-ablated motor neurons exhibit ALS-like degeneration and that ALS motor neurons reduce the proteasome activity (Jenkins et al, 2020), we assumed that ALS motor neurons lack proteasome-mediated stress responses at pre-symptomatic stage, similar to injury-induced *Rpt3*-deficient motor neurons. Previous reports demonstrated that pathological ALS motor neurons show similar multiple stress responses to injured motor neurons, including ATF3 induction (Lobsiger et al, 2007). Notably, ATF3-positive motor neurons increase in number along with disease progression, or under the manipulation of disease-associated genes such as TANK-binding kinase 1 (TBK1), although it is unclear whether ATF3 drives survival or cell death mechanisms in pathological damaged motor neurons (Vlug et al, 2005; Seijffers et al, 2014; Morisaki et al, 2016; Gerbino et al, 2020). In this study, *Atf3*;SOD1 mice permitted selective visualization of ATF3-positive motor neurons by GFP at the pre-symptomatic stage. ATF3 is required for axotomy-induced reprogramming of injured neurons (Chandran et al, 2016; Renthal et al, 2020). Therefore, GFP-inducing SOD1 motor neurons might attempt to initiate regeneration programs but failed it. One of the reasons of the failure would be the lack of proteasome-mediated stress responses, which was demonstrated in this study.

We describe here that the proteasome-mediated disassembly of the AIS could be a stress response, which is somehow missing in GFP-positive SOD1 motor neurons. We did not find a significant change in AIS lengths in SOD1 motor neurons, although a previous study showed slightly shorter AIS structures in ALS motor neurons (Bonnievie et al, 2020). Instead, we found that GFP-positive SOD1 motor neurons had fewer mitochondria in the AIS and a concomitantly reduced number of axonal mitochondria, similar to injury-induced *Rpt3*-ablated motor neurons. Previous study using electron microscopy suggested the possibility that mitochondrial transport was impaired at the proximal axon in SOD1^{G93A} mice and ALS patients (Sasaki & Iwata, 1996; Sasaki et al, 2005). Defective axonal transport of mitochondria is the earliest phenomena observed in ALS models and has been proposed to be causative in this disease (Magrane et al, 2014; Moller et al, 2017). *Atf3*;SOD1 mice and injury-induced *Rpt3* CKO mice showed the possibility that the failure of proteasome-mediated AIS disruption would cause a defective supply of mitochondria from the cell body to the axon, at least in ATF3-positive motor neurons. Lin et al (2017) have reported that mitochondria-anchoring protein syntrophin is involved in the removal of damaged mitochondria from axon at early pre-symptomatic stage (Lin et al, 2017). Therefore, ALS motor neurons might require the replenishment of healthy mitochondria to axons via AIS disassembly, in cooperation with the removal of damaged mitochondria.

Overall, our mouse model system using unique character of *Atf3* gene is a powerful tool for expanding our understanding of the molecular basis of damaged neurons prior to neurodegeneration. Using the system, we uncover the fundamental mechanism that the proteasome-dependent temporal breakdown of the AIS would be

beneficial for traumatically or pathologically damaged motor neurons to supply mitochondrial energy to damaged axon through the transition to an immature state. This transient proteasome-mediated

AIS disassembly could be a new machinery in the mitochondrial logistics system to keep the integrity of damaged motor neurons, and this system could be a new therapeutic target in ALS.

Materials and Methods

Reagents and Tools table

Reagent/Resource	Reference or Source	Identifier or Catalog Number
Experimental Models		
C57BL/6Ncr1 (Mus Musculus)	SLC	N/A
SJL/J (Mus Musculus)	Charles River	N/A
Atf3:BAC Tg (Mus Musculus)	Kiryu-Seo et al (2016)	N/A
Atf3:BAC2 Tg (Mus Musculus)	This paper	N/A
Rpt3-flox (Mus Musculus)	Tashiro et al (2012)	N/A
B6SJL-Tg(SOD1*G93A)1Gur/J (Mus Musculus)	The Jackson Laboratory	JAX stock # 002726; RRID: IMSR_JAX:002726
B6.Cg-Tg(Thy1-CFP/COX8A)S2Lich/J (Mus Musculus)	The Jackson Laboratory	IMSR Cat# JAX:007967, RRID:IMSR_JAX:007967
COS-7 cell	ATCC	Cat# CRL-1651
Recombinant DNA		
Unmodified BAC clone	The BACPAC Resources Center at the Children's Hospital Oakland Research Institute	RP24-318C6
Rat AnkG (1-438, 439-837, 838-1156, 1157-1476, 1477-1908, 1909-2325, 2326-2622 aa.) in pEF-BOS-GST	This paper	N/A
HA-Ubiquitin in pcDNA3	Addgene	Addgene plasmid 18712
MitoGFP-ires-Cre in pL451	Kiryu-Seo et al (2016)	N/A
Antibodies		
Rabbit anti-GFP polyclonal (1:1,000)	MBL	Cat# 598, RRID:AB_591819
Rat anti-GFP monoclonal (1:1,000)	Nacalai Tesque	Cat# 04404-84, RRID:AB_10013361
Rabbit anti-Ank-G (Ankirin-G) polyclonal (1:500)	Frontier Institute	Cat# AnkG-Rb, RRID:AB_2571661
Mouse anti-Ankyrin G Monoclonal (4G3F8) (1:300)	Thermo Fisher Scientific	Cat# 33-8800, RRID:AB_2533145
Rabbit anti-RPT3 polyclonal (1:500)	Enzo Life Sciences	Cat# BML-PW8175, RRID:AB_10541231
Rabbit anti-TARDBP polyclonal (1:500)	Proteintech	Cat# 10782-2-AP, RRID:AB_615042
Mouse anti-TARDBP monoclonal (1:500)	Novus	Cat# NBP1-92695, RRID:AB_11005586
Guinea pig anti-p62 polyclonal (1:500)	Progen	Cat# GP62-C, RRID:AB_2687531
Goat anti-ECEL1 (N-20) polyclonal (1:1,000)	Santa Cruz Biotechnology	Cat# sc-11338, RRID:AB_2097871
Mouse anti-NeuN monoclonal (1:1,000)	Millipore	Cat# MAB377, RRID:AB_2298772
Rabbit anti-ATF-3 (C-19) polyclonal (1:1,000)	Santa Cruz Biotechnology	Cat# sc-188, RRID:AB_2258513
Rabbit anti-ATF3 monoclonal (1:1,000)	Abcam	Abcam Cat# ab207434, RRID:AB_2734728
Goat anti-ChAT polyclonal (1:1,000)	Millipore	Cat# AB144P, RRID:AB_2079751
Rabbit anti-ChAT polyclonal (1:5,000)	Ichikawa et al (1997)	
Rabbit anti-Iba1 polyclonal (1:1,000)	Wako	Cat# 019-19741, RRID:AB_839504
Goat anti-GFAP polyclonal (1:1,000)	Abcam	Cat# ab53554, RRID:AB_880202
Rabbit anti-Caspr polyclonal (1:1,000)	Abcam	Cat# ab34151, RRID:AB_869934
Mouse anti-Neurofilament H monoclonal (1:1,000)	Covance	Cat# SMI-32P-100, RRID:AB_10719742
Mouse anti-cytochrome c monoclonal (1:500)	Thermo Fisher Scientific	Cat# 45-6100, RRID:AB_2533821
Goat anti-MMP-9 polyclonal (1:1,000)	Sigma-Aldrich	Cat# M9570, RRID:AB_1079397
Goat anti-Osteopontin polyclonal (1:1,000)	R and D Systems	Cat# AF808, RRID:AB_2194992
Rat anti-Lamp-1 monoclonal (1:1,000)	Santa Cruz Biotechnology	Cat# sc-19992, RRID:AB_2134495

Reagents and Tools table (continued)

Reagent/Resource	Reference or Source	Identifier or Catalog Number
Mouse anti-GAPDH Monoclonal (6C5) (1:5,000)	Thermo Fisher Scientific	Cat# AM4300, RRID:AB_2536381
α -Bungarotoxin, Alexa Fluor™ 594 conjugate (1:300)	ThermoFisher	B13423
GST-Tag Polyclonal (1:1,000)	MBL	Cat# PM013, RRID:AB_591789
Mouse Anti-HA.11 Monoclonal (1:1,000)	Covance	Cat# MMS-101P-1000, RRID:AB_291259
Alexa Donkey anti-rat 488 (1:500)	Thermo Fisher Scientific	Cat# A-21208, RRID:AB_2535794
Alexa Donkey anti-rabbit 488 (1:500)	Thermo Fisher Scientific	Cat# A-21206, RRID:AB_2535792
Alexa Donkey anti-rabbit 594 (1:500)	Thermo Fisher Scientific	Cat# A-21207, RRID:AB_14163
Alexa Donkey anti-mouse 594 (1:500)	Thermo Fisher Scientific	Cat# A-21203, RRID:AB_141633
Alexa Donkey anti-goat 647 (1:500)	Thermo Fisher Scientific	Cat# A-21447, RRID:AB_2535864
Alexa Goat anti-rat 488 (1:500)	Thermo Fisher Scientific	Cat# A-11006, RRID:AB_2534074
Alexa Goat anti-rabbit 594 (1:500)	Thermo Fisher Scientific	Cat# A-11012, RRID:AB_2534079
Alexa goat anti-mouse 594 (1:500)	Thermo Fisher Scientific	A-11005, RRID:AB_2534073
Alexa goat anti-guinea pig 594 (1:500)	Thermo Fisher Scientific	Cat# A-11076, RRID:AB_2534120
Oligonucleotides and sequence-based reagents		
See Appendix Table S1		
Chemicals, enzymes and other reagents		
ECL™ Prime Western Blotting System	Amersham	Cat# RPN2232
SuperSepTMAce	WAKO	Cat# 197-15011
RNeasy lipid tissue midi kit	QIAGEN	Cat# 74804
SuperScript® III RNase H-Reverse Transcriptase	Invitrogen	Cat# 18080-085
CUBIC-L	Tokyo Chemical Industry Co., Ltd.	Cat# T3740
CUIBC-R	Tokyo Chemical Industry Co., Ltd.	Cat# T3741
Mounting solution	Tokyo Chemical Industry Co., Ltd.	Cat# M3294
Fast SYBR™ Green Master Mix	Thermo Fisher Scientific	Cat# 4385616
Software		
Fiji	Image J	Fiji NIH http://fiji.sc/
GraphPad Prism version 7.0	Graphpad Software	GraphPad Prism version 7.0 GraphPad Software, Inc https://www.graphpad.com/scientificsoftware/
Imaris	Bitplane	Bitplane
Zen black and blue	Carl Zeiss	Zeiss
Other		
AAV9-AnkG shRNA-mCherry - shRNA sequence 5'-CGCTCCTATTAGATCTTC-3'	Vector builder	N/A
AAV9-scramble shRNA	Vector builder	N/A
Fv10i	Olympus	
Lightsheet 7	Carl Zeiss	
SpinSR	Olympus	

Methods and Protocols

Animals

All animal protocols were carried out in accordance with the Nagoya university animal committee guidelines for the care and use of laboratory animals and were approved by the Nagoya university institutional animal care and use committee. All possible efforts were made to minimize suffering. Mice were housed in standard

cages with *ad libitum* access to food and water under a 12-h light/dark cycle.

Atf3:BAC2 Tg mice were generated according to general bacterial artificial chromosome (BAC) modification protocols as previously described (Kiryu-Seo et al, 2016). The BAC clone RP24-318C6, containing the *Atf3* locus, was purchased from the BACPAC Resources Center at the Children's Hospital Oakland Research Institute (CHORI) (BPRC, California, USA). Briefly, a gene fragment of GFP from

Aequorea coerulescens (AcGFP) attached to the mitochondrial targeting sequence of cytochrome c oxidase subunit VIII, followed by an IRES, cre recombinase and SV40-polyA, was inserted into PL451 in front of the FRT-Neo-FRT cassette. The initiation codon of *Atf3* gene in BAC was replaced by that of GFP with the mitochondrial targeting sequence. BAC DNA was purified and injected into pronuclei from C57BL/6 oocytes (Institute of Immunology Co., Ltd., Tochigi, Japan) to generate Tg mice. The *Atf3*:BAC2 Tg mice were crossed with C57BL/6Ncr mice for at least seven generations. The hemizygous mice were fertile and viable without neurological abnormalities.

To generate injury-induced *Rpt3* CKO mice (*Atf3*:BAC2;*Rpt3*^{fllox/fllox}), we carefully optimized cell-type-specific recombination (Luo et al, 2020). We crossed *Atf3*:BAC2 Tg mice with *Rpt3*^{fllox/fllox} mice and maintained the colony as heterozygous *Atf3*:BAC2;*Rpt3*^{fllox/+} mice. *Rpt3*^{fllox/fllox} mice were provided by Drs. Tashiro and Takahashi (Kyoto University). Heterozygous *Atf3*:BAC2;*Rpt3*^{fllox/+} mice were bred with homozygous *Rpt3*^{fllox/fllox} mice to generate injury-induced *Rpt3* CKO mice (*Atf3*:BAC2;*Rpt3*^{fllox/fllox}; Fig EV1E–H). Homozygous *Rpt3*^{fllox/fllox} mice were always maintained by crossing with *Rpt3*^{fllox/fllox}, which had not crossed with cre driver mice to avoid unexpected germline recombination.

Thy1-Mito mice were purchased from Jackson Laboratory (Bar Harbor, ME; B6.Cg-Tg (Thy1-CFP/COX8A) S2Lich/J Stock No: 007967) and were maintained as a hemizygous colony.

To generate *Atf3*:BAC; SOD1^{G93A} (*Atf3*:SOD1) mice, we initially crossed male SJL/J mice with female *Atf3*:BAC Tg mice (C57BL/6 background) which we reported previously (Kiryu-Seo et al, 2016) and obtained *Atf3*:BAC Tg mice with B6SJL background. The SOD1^{G93A} mice (B6SJL-Tg(SOD1*G93A)1Gur/J, stock number 002726, B6SJL background, Jackson Laboratory, Bar Harbor, ME) were crossed with *Atf3*:BAC Tg mice with B6SJL background to generate *Atf3*:SOD1 mice (Fig EV5A).

All mice were matched for age and sex. Experiments were performed on both sexes, with the exception of experiments involving *Atf3*:SOD1 mice. Male *Atf3*:SOD1 mice and the male littermates carrying only *Atf3*:BAC transgene were used for experiment. Primer sequences for genotyping of *Atf3*:BAC Tg, *Atf3*:BAC2 Tg and *Rpt3*^{fllox/fllox} mice are described in Appendix Table S1. Primer sequences and protocol for genotyping of *Thy1*-Mito and SOD1^{G93A} mice are available through the Jackson Laboratory.

Surgical procedures

Animals of either sex at 8–10 weeks old were anesthetized under isoflurane. For hypoglossal nerve injury, the right hypoglossal nerve was carefully exposed under the digastric muscle and transected with a pair of scissors. The skin was closed with sutures. For sciatic nerve injury, the right sciatic nerve was exposed in the mid-thigh level. The nerve was carefully freed from surrounding connective tissue and then cut with a pair of scissors. The skin was closed with sutures.

Immunohistochemistry

Mice were perfused transcardially with 1% paraformaldehyde (PFA) in PB containing 0.2% picric acid. Brains, spinal cords, nerves, and tongues were removed, post-fixed, and then transferred to 30% sucrose solution. For immunohistochemistry using DINE antibody, mice were decapitated and the brains were freshly frozen in powdered dry ice. Both perfused and fresh frozen samples were

embedded in OCT compound and cut into serial 16- μ m-thick sections on a cryostat. Fresh frozen sections were fixed in 4% PFA for 10 min before immunohistochemical procedures. Both sections were washed in 0.01 M PBS, blocked in 0.01 M PBS containing 1% BSA and 0.3% Triton, and incubated with following primary antibodies; anti-ATF3 (Santa Cruz, 1:1,000, Cat# sc-188, RRID: AB_2258513), anti-RPT3 (Enzo Life Sciences, 1:500, Cat# BML-PW8175, RID:AB_10541231), anti-GFP (Nacalai, 1:1,000, Cat# 04404-84, RID:AB_10013361 or MBL, 1:1,000, Cat# 598, RRID: AB_591819), anti-Iba1 (WAKO, 1:1,000, Cat# 019-19741, RRID: AB_839504), anti-p62 (Progen, 1:500, Cat# GP62-C, RRID: AB_2687531), anti-TDP-43 (Proteintech, 1:500, Cat# 10782-2-AP, RRID:AB_615042 or Novus, 1:500, Cat# NBP1-92695, RRID: AB_11005586), anti-AnkG (Frontier Institute, 1:500, Cat# AnkG-Rb, RRID:AB_2571661 or Thermo Fisher Scientific, 1:300, Cat# 33-8800, RRID:AB_2533145), anti-Caspr (Abcam, 1:1,000, Cat# ab34151, RRID:AB_869934), anti-NeuN (Millipore, 1:1,000, Cat# MAB377, RRID:AB_2298772), anti-DINE/ ECEL1 (1:1,000, Cat# sc-11,338, RRID:AB_2097871), anti-cytochrome c (Thermo Fisher Scientific, 1:500, Cat# 45-6100, RRID:AB_2533821), anti-GFAP (Abcam, 1:1,000, Cat# ab53554, RRID:AB_880202), anti-MMP-9 (Sigma-Aldrich, 1:500, Cat# M9570, RRID:AB_1079397), anti-Osteopontin (R and D systems, 1:1,000, Cat# AF808, RRID:AB_2194992), anti-Neurofilament (Covance, 1:1,000, Cat# SMI-32P-100, RRID: AB_10719742), anti-Lamp1 (Santa Cruz Biotechnology, 1:1,000, Cat# sc-19992, RRID:AB_2134495), anti-ChAT antibody (Millipore, 1:1,000, Cat# AB144P, RRID:AB_2079751) and Rabbit anti-ChAT antibody provided by Dr. Misawa (Keio University) (Ichikawa et al, 1997). After washing with PBS, sections were incubated with secondary antibodies: AlexaFluor 488, 594, or 647 (Life Technologies, 1:500) or AlexaFluor 594-conjugated α -Bungarotoxin (Thermo Fisher, 1:300, cat# B13423). Images were acquired on a confocal laser scanning microscope (Olympus FV10i, Tokyo, Japan) using x10 objective or $\times 60$ water-immersion objective (NA1.2).

Tissue clearing

After mice were perfused transcardially with 4% PFA-PBS, brain and spinal cord were dissected, washed with PBS, and processed according to CUBIC protocol (Tainaka et al, 2018). The samples were immersed in 1:1 water-diluted CUBIC-L (Tokyo Chemical Industry, M0374) for 1 day and then incubated with CUBIC-L with gentle shaking at 37°C for 4–5 days. After washing with PBS, the samples were immersed in 1:1 water-diluted CUBIC-R for 1 day and then in CIBUC-R with gentle shaking at room temperature for 1–2 days.

Lightsheet microscopy

The images are acquired with lightsheet 7 microscope (Zeiss, Germany). For CUBIC treated brain and spinal cord, images were captured using a 5 \times objective lens with digital zoom from 0.8 \times to 2.5 \times with digital zoom equipped with laser emitting 488 nm. The RI-matched sample was immersed in an oil mixture (RI = 1.525). Raw data were handled using a ZEISS Zen blue and black. 3D images were created in Imaris (Bitplane, Oxford Instruments, Belfast, UK).

Counting of motor neurons

For quantification of cell survival after axotomy, sections were stained with thionine. Thionine-stained hypoglossal motor neurons in injured and control sides were counted separately and at the

identical level between animals as previously described (Kiryu-Seo et al, 2005). Data were presented as the percentage of surviving neurons on the injured side, compared with neurons on control side. For cell survival of GFP-positive injured motor neurons, the number of GFP-positive injured hypoglossal motor neurons at 5 days after injury was counted while that of ChAT-positive uninjured hypoglossal motor neurons was counted at the identical level between animals. Data were presented as the percentage of GFP-positive injured motor neurons compared with ChAT-positive uninjured motor neurons. For the cell number of uninjured hypoglossal motor neurons, ChAT-positive motor neurons in hypoglossal nucleus were counted at the identical level between animals. Data were shown as the cell number of unilateral hypoglossal nucleus per section. For counting GFP-positive hypoglossal motor neurons in transparent 3D images, serial 2D slices were used and motor neurons were carefully identified. Data were shown as the total number of GFP-positive motor neurons in hypoglossal nucleus.

RNA isolation and quantitative reverse-transcription PCR

Contralateral and ipsilateral hypoglossal nuclei at 5 days after injury were dissected from 7–10 mice. Total RNA was extracted using an RNeasy Lipid Tissue kit (Qiagen, Hilden, Germany) according to the manufacturer's instructions. cDNA was synthesized using SuperscriptIII (Thermo Fisher Scientific, Massachusetts, USA) following the standard protocols. Quantitative PCR was performed on the StepOnePlus™ Real-Time PCR System using primer pairs and SYBR Green PCR Master Mix (Thermo Fisher Scientific). Data were normalized to the GAPDH levels and calculated using the comparative threshold cycle method. Primer sequences are described in Appendix Table S1.

Immunoblotting

Contralateral and ipsilateral hypoglossal nuclei and nerves from 5–7 mice were dissected and homogenized in lysis buffer A containing 150 mM NaCl, 20 mM Tris-HCl (pH 7.5), 10 mM EDTA, 1% NP-40, 0.5% deoxycholate, 0.1% SDS, 5 µg/ml aprotinin, 1 mM PMSF, and 1 µg/ml leupeptin and centrifuged to collect the supernatant. Proteins were resolved by SDS-PAGE using 4–12% Bis-Tris gels (FUJIFILM Wako pure chemical corporation, Japan) and were transferred to PVDF membranes. Anti-AnkG (Frontier Institute, Cat# AnkG-Rb, RRID:AB_2571661), anti-RPT3 (Enzo Life Sciences, Cat# BML-PW8175, RRID:AB_10541231) and anti-GAPDH (Thermo Fisher Scientific, Cat# AM4300, RRID:AB_2536381) primary antibodies and were diluted 1:1,000–1:5,000. Signals were detected using ECL (GE Healthcare, Chicago, USA).

Ubiquitination assay

The cDNA fragments encoding truncated forms of rat AnkG were subcloned into pEF-BOS vector. Each GST-tagged AnkG plasmid and HA-tagged ubiquitin in pcDNA3 (addgene18712) were cotransfected into COS-7 cells. At 18 h after transfection, the cells were treated with 25 µM ALLN (Calbiochem, Merck, Darmstadt, Germany) for 6 h. The cells were lysed in lysis buffer B (20 mM Tris-HCl, pH 7.5, 1 mM EDTA, 100 mM NaCl, 0.5% NP-40 substitute, 1 mM DTT, 25 µM ALLN, 0.5 mM phenylmethylsulfonyl fluoride, 2 µg/ml aprotinin, 1 µg/ml leupeptin, 2 µg/ml antipain, and 10 µg/ml benzamide). The cell lysates were incubated with Glutathione Sepharose 4B beads (GE Healthcare, Chicago, USA) for 2 h at 4°C,

and the beads were subsequently washed three times with lysis buffer B. After washing, the beads were resuspended with SDS-PAGE sample buffer, and the samples were subjected to immunoblot analysis using anti-HA (Covance, Cat# MMS-101P-1000, RRID:AB_291259) and anti-GST (MBL, Cat# PM013, RRID:AB_591789) antibodies.

Image analysis of the fluorescently labeled AIS and mitochondria

All image analysis studies including length and number of the AIS, intensity ratio of GFP in the AIS, and fluorescent line intensity plots were performed by using Fiji software (NIH, Bethesda, MD, USA). Images were acquired on a confocal laser scanning microscope (Olympus FV10i, Tokyo, Japan) using a ×60 water-immersion objective (NA1.2). The length and number of AIS stained by AnkG was measured using z-stacked images. The number of the AIS per area with 1,024 × 1,024 pixel was counted. 20–30 neurons for AIS length and 3–6 areas for AIS number were measured in each mouse. For fluorescent intensity of GFP in the AIS region, we traced the line along the AIS region and subtracted the random fluorescence intensity in these images, to control for background signals. The mean intensities of GFP in the AIS were averaged and presented as the percentage of the intensity from *Thy1-Mito* mouse. 10–20 neurons from each mouse were measured. For fluorescent line intensity, the fluorescent intensity of GFP and AnkG in the AIS was plotted from the cell body to the axon along 1-µm-wide lines. Representative images and their corresponding plots are shown in figures. The disappeared AIS region after injury was identified when injured motor neurons retained very weak or fragmented signal of AnkG or when injured motor neuron extended the neurite, which exited hypoglossal nucleus and formed hypoglossal nerve bundle.

Super-resolution images of mitochondria in injured motor neurons were acquired by SpinSR10 (Olympus, Tokyo, Japan) using a ×100 oil-immersion objective and deconvoluted. A single layer with highest resolution in the images was selected, and the fluorescent intensity of GFP in cell body was plotted along the line. Each peak represents the existence of mitochondria on a line within soma. The number of peaks on a line was counted as mitochondrial number from 5–7 neurons from each mouse.

In vivo imaging

Mice of either sex at 8–10 weeks old were anesthetized by i.p. injection of pentobarbital (45 mg/kg). To image axonal mitochondria in the sciatic nerve, we surgically exposed the uninjured and injured sciatic nerve without causing damage and positioned the mouse on an inverted laser scanning confocal microscope (Olympus FV10i) equipped with a temperature-controlled chamber at 37°C. Time-lapse movies were acquired on a confocal microscope equipped with a temperature-controlled stage at 37°C and with a ×60 water-immersion objective (NA1.2) (Olympus FV10i). Images were captured every 5 s and 100 frames were acquired in total for each recording, with laser power set to < 30% to minimize damage. Time-lapse images of mitochondrial dynamics were collected in a single focal plane at 1,024 × 1,024 pixel.

Quantification of axonal mitochondria

For whole-mount observation of mitochondria in nerves, hypoglossal and sciatic nerves were removed from mice, which were perfused transcardially with 4% paraformaldehyde (PFA) in

PB. Subsequently, images of whole-mount axon were acquired on a confocal laser scanning microscope using $\times 60$ water-immersion objective (Olympus FV10i). Digital Z stack images were obtained with sequential acquisition setting. The number of mitochondria in a single axon was counted using Fiji software. Data were presented as mitochondrial number in $50 \mu\text{m}^2$ of axon. A 5–8 axons from each mouse were used for counting. To quantify mobile and stationary mitochondria, kymographs were generated using the Fiji software (NIH, Bethesda, MD, USA) as described previously (Kiryu-Seo *et al*, 2010). Motile mitochondria appeared as diagonal lines. Each mobile mitochondrion confirmed to be moving for six or more consecutive frames within the area was measured. Stationary mitochondrial sites were identified as vertical lines on the kymographs. The percentage of motile mitochondria of total mitochondria is defined in a given distance for 180 s per axons. Stationary mitochondria were counted per given distance of axon.

Adeno-associated viruses (AAVs)

The shRNA of AnkG was cloned into pAAV vector with the sequence, GCGTCTCCTATTAGATCTTTC, targeting a serine-rich region shared by both the 270-kDa and 480-kDa isoforms of mouse AnkG (Ye *et al*, 2020), followed by PGK promoter and mCherry (VectorBuilder, Chicago, USA). The scrambled shRNA followed by PGK promoter and mCherry was purchased from VectorBuilder. The plasmids were transfected into 293 cells to produce AAVs carrying serotype 9. The titers of all viral preparations were at least 1.0×10^{13} GC/ml. The AAVs were injected into the tongue of 6–8-week-old mice using Hamilton syringe at 3–4 weeks before hypoglossal nerve injury.

Statistical analysis

Results are expressed as mean \pm SEM. Statistical analysis was performed using Prism7 (GraphPad software). Unpaired *t*-test was used to compare two groups. One-way ANOVA was used for multiple comparisons, followed by *Tukey post hoc* analysis. Survival data were analyzed by long-rank test. *P*-values < 0.05 were considered significant.

Data availability

This study includes no data deposited in external repositories.

Expanded View for this article is available online.

Acknowledgments

We appreciate Ayako Asano and Yoshiko Itai for managing the project. We thank Naomi Tawarayama and Kyoko Muraki for excellent technical assistance. We thank Chenmin Li and Hiromi Tamada for sharing data. We thank Hideo Misawa (Keio University) for providing rabbit ChAT antibody. We acknowledge staffs of Division of Experimental Animals, Nagoya University Graduate School of Medicine and staffs of the Nagoya University Equipment Sharing system for their technical support. We are also grateful to Hiroshi Kuba and Rei Yamada (Nagoya University, Japan) for their useful comments, and Matthew N. Rasband (Baylor College of Medicine, USA) for critical reading of our manuscript. We thank Edanz (<https://jp.edanz.com/ac>) for editing a draft of this manuscript. This work was supported by JSPS KAKENHI (25430036,

18H02524 and 21K19310) to S. K.-S., TOYOAKI SCHOLARSHIP FOUNDATION to S. K.-S. and JSPS KAKENHI (16H05117 and 22H03437) to H.K.

Author contributions

Sumiko Kiryu-Seo: Conceptualization; resources; data curation; formal analysis; supervision; funding acquisition; validation; investigation; visualization; writing – original draft; writing – review and editing. **Reika Matsushita:** Data curation; formal analysis; investigation. **Yoshitaka Tashiro:** Resources; writing – review and editing. **Takeshi Yoshimura:** Data curation; formal analysis; investigation; writing – review and editing. **Yohei Iguchi:** Resources; writing – review and editing. **Masahisa Katsuno:** Resources; writing – review and editing. **Ryosuke Takahashi:** Resources; writing – review and editing. **Hiroshi Kiyama:** Conceptualization; supervision; funding acquisition; writing – review and editing.

Disclosure and competing interests statement

The authors declare that they have no conflict of interest.

References

- An D, Fujiki R, Iannitelli DE, Smerdon JW, Maity S, Rose MF, Gelber A, Wanaselja EK, Yagudayeva I, Lee JY *et al* (2019) Stem cell-derived cranial and spinal motor neurons reveal proteostatic differences between ALS resistant and sensitive motor neurons. *Elife* 8: e44423
- Baalman K, Marin MA, Ho TS, Godoy M, Cherian L, Robertson C, Rasband MN (2015) Axon initial segment-associated microglia. *J Neurosci* 35: 2283–2292
- Benned-Jensen T, Christensen RK, Denti F, Perrier JF, Rasmussen HB, Olesen SP (2016) Live imaging of Kv7.2/7.3 cell surface dynamics at the axon initial segment: high steady-state stability and calpain-dependent excitotoxic downregulation revealed. *J Neurosci* 36: 2261–2266
- van Beuningen SFB, Will L, Harterink M, Chazneau A, van Battum EY, Frias CP, Franker MAM, Katrukha EA, Stucchi R, Vocking K *et al* (2015) TRIM46 controls neuronal polarity and axon specification by driving the formation of parallel microtubule arrays. *Neuron* 88: 1208–1226
- Bilsland LG, Sahai E, Kelly G, Golding M, Greensmith L, Schiavo G (2010) Deficits in axonal transport precede ALS symptoms *in vivo*. *Proc Natl Acad Sci U S A* 107: 20523–20528
- Bonnevie VS, Dimintyanova KP, Hedegaard A, Lehnhoff J, Grondahl L, Moldovan M, Meehan CF (2020) Shorter axon initial segments do not cause repetitive firing impairments in the adult presymptomatic G127X SOD-1 amyotrophic lateral sclerosis mouse. *Sci Rep* 10: 1280
- Bradke F, Di Giovanni S, Fawcett J (2020) Neuronal maturation: challenges and opportunities in a nascent field. *Trends Neurosci* 43: 360–362
- Cartoni R, Norsworthy MW, Bei F, Wang C, Li S, Zhang Y, Gabel CV, Schwarz TL, He Z (2016) The mammalian-specific protein Armcx1 regulates mitochondrial transport during axon regeneration. *Neuron* 92: 1294–1307
- Chamberlain KA, Sheng ZH (2019) Mechanisms for the maintenance and regulation of axonal energy supply. *J Neurosci Res* 97: 897–913
- Chandran V, Coppola G, Nawabi H, Omura T, Versano R, Huebner EA, Zhang A, Costigan M, Yekkirala A, Barrett L *et al* (2016) A systems-level analysis of the peripheral nerve intrinsic axonal growth program. *Neuron* 89: 956–970
- Farias GG, Guardia CM, Britt DJ, Guo X, Bonifacino JS (2015) Sorting of dendritic and axonal vesicles at the pre-axonal exclusion zone. *Cell Rep* 13: 1221–1232
- Gerbino V, Kaunga E, Ye J, Canzio D, O'Keefe S, Rudnick ND, Guarnieri P, Lutz CM, Maniatis T (2020) The loss of TBK1 kinase activity in motor neurons

- or in all cell types differentially impacts ALS disease progression in SOD1 mice. *Neuron* 106: 789–805.e785
- Gumy LF, Katrukha EA, Grigoriev I, Jaarsma D, Kapitein LC, Akhmanova A, Hoogenraad CC (2017) MAP2 defines a pre-axonal filtering zone to regulate KIF1- versus KIF5-dependent cargo transport in sensory neurons. *Neuron* 94: 347–362.e7
- Hamdan H, Lim BC, Torii T, Joshi A, Konning M, Smith C, Palmer DJ, Ng P, Leterrier C, Oses-Prieto JA et al (2020) Mapping axon initial segment structure and function by multiplexed proximity biotinylation. *Nat Commun* 11: 100
- Han SM, Baig HS, Hammarlund M (2016) Mitochondria localize to injured axons to support regeneration. *Neuron* 92: 1308–1323
- Han Q, Xie Y, Ordaz JD, Huh AJ, Huang N, Wu W, Liu N, Chamberlain KA, Sheng ZH, Xu XM (2020) Restoring cellular energetics promotes axonal regeneration and functional recovery after spinal cord injury. *Cell Metab* 31: 623–641.e8
- Hellal F, Hurtado A, Ruschel J, Flynn KC, Laskowski CJ, Umlauf M, Kapitein LC, Strikis D, Lemmon V, Bixby J et al (2011) Microtubule stabilization reduces scarring and causes axon regeneration after spinal cord injury. *Science* 331: 928–931
- Huang CY, Rasband MN (2018) Axon initial segments: structure, function, and disease. *Ann N Y Acad Sci* 1420: 46–61
- Ichikawa T, Ajiki K, Matsuura J, Misawa H (1997) Localization of two cholinergic markers, choline acetyltransferase and vesicular acetylcholine transporter in the central nervous system of the rat: In situ hybridization histochemistry and immunohistochemistry. *J Chem Neuroanat* 13: 23–39
- Jenkins PM, Kim N, Jones SL, Tseng WC, Svitkina TM, Yin HH, Bennett V (2015) Giant ankyrin-G: a critical innovation in vertebrate evolution of fast and integrated neuronal signaling. *Proc Natl Acad Sci U S A* 112: 957–964
- Jenkins EC, Shah N, Gomez M, Casalena G, Zhao D, Kenny TC, Guariglia SR, Manfredi G, Germain D (2020) Proteasome mapping reveals sexual dimorphism in tissue-specific sensitivity to protein aggregations. *EMBO Rep* 21: e48978
- Kabashi E, Agar JN, Strong MJ, Durham HD (2012) Impaired proteasome function in sporadic amyotrophic lateral sclerosis. *Amyotroph Lateral Scler* 13: 367–371
- Kalinski AL, Kar AN, Craver J, Tosolini AP, Sleight JN, Lee SJ, Hawthorne A, Brito-Vargas P, Miller-Randolph S, Passino R et al (2019) Deacetylation of Miro1 by HDAC6 blocks mitochondrial transport and mediates axon growth inhibition. *J Cell Biol* 218: 1871–1890
- Kaplan A, Spiller KJ, Towne C, Kanning KC, Choe GT, Geber A, Akay T, Aebischer P, Henderson CE (2014) Neuronal matrix metalloproteinase-9 is a determinant of selective neurodegeneration. *Neuron* 81: 333–348
- Kiryu-Seo S, Kiyama H (2011) The nuclear events guiding successful nerve regeneration. *Front Mol Neurosci* 4: 53
- Kiryu-Seo S, Hirayama T, Kato R, Kiyama H (2005) Noxa is a critical mediator of p53-dependent motor neuron death after nerve injury in adult mouse. *J Neurosci* 25: 1442–1447
- Kiryu-Seo S, Gamo K, Tachibana T, Tanaka K, Kiyama H (2006) Unique anti-apoptotic activity of EAAC1 in injured motor neurons. *EMBO J* 25: 3411–3421
- Kiryu-Seo S, Kato R, Ogawa T, Nakagomi S, Nagata K, Kiyama H (2008) Neuronal injury-inducible gene is synergistically regulated by ATF3, c-Jun, and STAT3 through the interaction with Sp1 in damaged neurons. *J Biol Chem* 283: 6988–6996
- Kiryu-Seo S, Ohno N, Kidd GJ, Komuro H, Trapp BD (2010) Demyelination increases axonal stationary mitochondrial size and the speed of axonal mitochondrial transport. *J Neurosci* 30: 6658–6666
- Kiryu-Seo S, Tamada H, Kato Y, Yasuda K, Ishihara N, Nomura M, Mihara K, Kiyama H (2016) Mitochondrial fission is an acute and adaptive response in injured motor neurons. *Sci Rep* 6: 28331
- Kong G, Zhou L, Serger E, Palmisano I, De Virgiliis F, Hutson TH, McLachlan E, Freiwald A, La Montanara P, Shkura K et al (2020) AMPK controls the axonal regenerative ability of dorsal root ganglia sensory neurons after spinal cord injury. *Nat Metab* 2: 918–933
- Kuijpers M, van de Willige D, Freal A, Chazeau A, Franker MA, Hofenk J, Rodrigues RJ, Kapitein LC, Akhmanova A, Jaarsma D et al (2016) Dynein regulator NDEL1 controls polarized cargo transport at the axon initial segment. *Neuron* 89: 461–471
- Leterrier C (2018) The axon initial segment: An updated viewpoint. *J Neurosci* 38: 2135–2145
- Lewis TL Jr, Turi GF, Kwon SK, Losonczy A, Polleux F (2016) Progressive decrease of mitochondrial motility during maturation of cortical axons *in vitro* and *in vivo*. *Curr Biol* 26: 2602–2608
- Licht-Mayer S, Campbell GR, Canizares M, Mehta AR, Gane AB, McGill K, Ghosh A, Fullerton A, Menezes N, Dean J et al (2020) Enhanced axonal response of mitochondria to demyelination offers neuroprotection: Implications for multiple sclerosis. *Acta Neuropathol* 140: 143–167
- Lin MY, Cheng XT, Tamminen P, Xie Y, Zhou B, Cai Q, Sheng ZH (2017) Releasing syntaphilin removes stressed mitochondria from axons independent of mitophagy under pathophysiological conditions. *Neuron* 94: 595–610.e6
- Lobsiger CS, Boillee S, Cleveland DW (2007) Toxicity from different SOD1 mutants dysregulates the complement system and the neuronal regenerative response in ALS motor neurons. *Proc Natl Acad Sci U S A* 104: 7319–7326
- Lu Y, Brommer B, Tian X, Krishnan A, Meer M, Wang C, Vera DL, Zeng Q, Yu D, Bonkowski MS et al (2020) Reprogramming to recover youthful epigenetic information and restore vision. *Nature* 588: 124–129
- Luo L, Ambrozkiwicz MC, Benseler F, Chen C, Dumontier E, Falkner S, Furlanis E, Gomez AM, Hoshina N, Huang WH et al (2020) Optimizing nervous system-specific gene targeting with Cre driver lines: Prevalence of germline recombination and influencing factors. *Neuron* 106: 37–65.e5
- Magrane J, Cortez C, Gan WB, Manfredi G (2014) Abnormal mitochondrial transport and morphology are common pathological denominators in SOD1 and TDP43 ALS mouse models. *Hum Mol Genet* 23: 1413–1424
- Maor-Nof M, Shipony Z, Lopez-Gonzalez R, Nakayama L, Zhang YJ, Couthouis J, Blum JA, Castruita PA, Linares GR, Ruan K et al (2021) p53 is a central regulator driving neurodegeneration caused by C9orf72 poly(PR). *Cell* 184: 689–708.e20
- Marin MA, de Lima S, Gilbert HY, Giger RJ, Benowitz L, Rasband MN (2016) Reassembly of excitable domains after CNS axon regeneration. *J Neurosci* 36: 9148–9160
- Misgeld T, Kerschensteiner M, Bareyre FM, Burgess RW, Lichtman JW (2007) Imaging axonal transport of mitochondria *in vivo*. *Nat Methods* 4: 559–561
- Moller A, Bauer CS, Cohen RN, Webster CP, De Vos KJ (2017) Amyotrophic lateral sclerosis-associated mutant SOD1 inhibits anterograde axonal transport of mitochondria by reducing Miro1 levels. *Hum Mol Genet* 26: 4668–4679
- Morisaki Y, Niikura M, Watanabe M, Onishi K, Tanabe S, Moriwaki Y, Okuda T, Ohara S, Murayama S, Takao M et al (2016) Selective expression of Osteopontin in ALS-resistant motor neurons is a critical determinant of late phase neurodegeneration mediated by matrix Metalloproteinase-9. *Sci Rep* 6: 27354

- Nakagomi S, Suzuki Y, Namikawa K, Kiryu-Seo S, Kiyama H (2003) Expression of the activating transcription factor 3 prevents c-Jun N-terminal kinase-induced neuronal death by promoting heat shock protein 27 expression and Akt activation. *J Neurosci* 23: 5187–5196
- Nijssen J, Comley LH, Hedlund E (2017) Motor neuron vulnerability and resistance in amyotrophic lateral sclerosis. *Acta Neuropathol* 133: 863–885
- Palmisano I, Danzi MC, Hutson TH, Zhou L, McLachlan E, Serger E, Shkura K, Srivastava PK, Hervera A, Neill NO et al (2019) Epigenomic signatures underpin the axonal regenerative ability of dorsal root ganglia sensory neurons. *Nat Neurosci* 22: 1913–1924
- Patodia S, Raivich G (2012) Role of transcription factors in peripheral nerve regeneration. *Front Mol Neurosci* 5: 8
- Patron LA, Zinsmaier KE (2016) Mitochondria on the road to power axonal regeneration. *Neuron* 92: 1152–1154
- Renthal W, Tochitsky I, Yang L, Cheng YC, Li E, Kawaguchi R, Geschwind DH, Woolf CJ (2020) Transcriptional reprogramming of distinct peripheral sensory neuron subtypes after axonal injury. *Neuron* 108: 128–144.e9
- Rudnick ND, Griffey CJ, Guarnieri P, Gerbino V, Wang X, Piersaint JA, Tapia JC, Rich MM, Maniatis T (2017) Distinct roles for motor neuron autophagy early and late in the SOD1(G93A) mouse model of ALS. *Proc Natl Acad Sci U S A* 114: E8294–E8303
- Sakao Y, Kawai T, Takeuchi O, Copeland NG, Gilbert DJ, Jenkins NA, Takeda K, Akira S (2000) Mouse proteasomal ATPases Psmc3 and Psmc4: Genomic organization and gene targeting. *Genomics* 67: 1–7
- Sasaki S, Iwata M (1996) Impairment of fast axonal transport in the proximal axons of anterior horn neurons in amyotrophic lateral sclerosis. *Neurology* 47: 535–540
- Sasaki S, Warita H, Abe K, Iwata M (2005) Impairment of axonal transport in the axon hillock and the initial segment of anterior horn neurons in transgenic mice with a G93A mutant SOD1 gene. *Acta Neuropathol* 110: 48–56
- Saxena S, Cabuy E, Caroni P (2009) A role for motoneuron subtype-selective ER stress in disease manifestations of FALS mice. *Nat Neurosci* 12: 627–636
- Schafer DP, Jha S, Liu F, Akella T, McCullough LD, Rasband MN (2009) Disruption of the axon initial segment cytoskeleton is a new mechanism for neuronal injury. *J Neurosci* 29: 13242–13254
- Seiffers R, Allchorne AJ, Woolf CJ (2006) The transcription factor ATF-3 promotes neurite outgrowth. *Mol Cell Neurosci* 32: 143–154
- Seiffers R, Zhang J, Matthews JC, Chen A, Tamrazian E, Babaniyi O, Selig M, Hynnen M, Woolf CJ, Brown RH Jr (2014) ATF3 expression improves motor function in the ALS mouse model by promoting motor neuron survival and retaining muscle innervation. *Proc Natl Acad Sci U S A* 111: 1622–1627
- Sleigh JN, Rossor AM, Fellows AD, Tosolini AP, Schiavo G (2019) Axonal transport and neurological disease. *Nat Rev Neurol* 15: 691–703
- Sohn PD, Huang CT, Yan R, Fan L, Tracy TE, Camargo CM, Montgomery KM, Arhar T, Mok SA, Freilich R et al (2019) Pathogenic tau impairs axon initial segment plasticity and excitability homeostasis. *Neuron* 104: 458–470.e5
- Sun S, Sun Y, Ling SC, Ferraiuolo L, McAlonis-Downes M, Zou Y, Drenner K, Wang Y, Ditsworth D, Tokunaga S et al (2015) Translational profiling identifies a cascade of damage initiated in motor neurons and spreading to glia in mutant SOD1-mediated ALS. *Proc Natl Acad Sci U S A* 112: E6993–E7002
- Tainaka K, Murakami TC, Susaki EA, Shimizu C, Saito R, Takahashi K, Hayashi-Takagi A, Sekiya H, Arima Y, Nojima S et al (2018) Chemical landscape for tissue clearing based on hydrophilic reagents. *Cell Rep* 24: 2196–2210.e9
- Tamada H, Kiryu-Seo S, Sawada S, Kiyama H (2021) Axonal injury alters the extracellular glial environment of the axon initial segment and allows substantial mitochondrial influx into axon initial segment. *J Comp Neurol* 529: 3621–3632
- Tashiro Y, Urushitani M, Inoue H, Koike M, Uchiyama Y, Komatsu M, Tanaka K, Yamazaki M, Abe M, Misawa H et al (2012) Motor neuron-specific disruption of proteasomes, but not autophagy, replicates amyotrophic lateral sclerosis. *J Biol Chem* 287: 42984–42994
- Taylor JP, Brown RH Jr, Cleveland DW (2016) Decoding ALS: from genes to mechanism. *Nature* 539: 197–206
- Tyzack GE, Hall CE, Sibley CR, Cymes T, Forostyak S, Carlino G, Meyer IF, Schiavo G, Zhang SC, Gibbons GM et al (2017) A neuroprotective astrocyte state is induced by neuronal signal EphB1 but fails in ALS models. *Nat Commun* 8: 1164
- Udan-Johns M, Bengoechea R, Bell S, Shao J, Diamond MI, True HL, Weihl CC, Baloh RH (2014) Prion-like nuclear aggregation of TDP-43 during heat shock is regulated by HSP40/70 chaperones. *Hum Mol Genet* 23: 157–170
- Ugun-Klusek A, Tatham MH, Elkharaz J, Constantin-Teodosiu D, Lawler K, Mohamed H, Paine SM, Anderson G, John Mayer R, Lowe J et al (2017) Continued 26S proteasome dysfunction in mouse brain cortical neurons impairs autophagy and the Keap1-Nrf2 oxidative defence pathway. *Cell Death Dis* 8: e2531
- Vlug AS, Teuling E, Haasdijk ED, French P, Hoogenraad CC, Jaarsma D (2005) ATF3 expression precedes death of spinal motoneurons in amyotrophic lateral sclerosis-SOD1 transgenic mice and correlates with c-Jun phosphorylation, CHOP expression, somato-dendritic ubiquitination and Golgi fragmentation. *Eur J Neurosci* 22: 1881–1894
- Webster CP, Smith EF, Shaw PJ, De Vos KJ (2017) Protein homeostasis in amyotrophic lateral sclerosis: Therapeutic opportunities? *Front Mol Neurosci* 10: 123
- Yamada R, Kuba H (2016) Structural and functional plasticity at the axon initial segment. *Front Cell Neurosci* 10: 250
- Ye J, Li J, Ye F, Zhang Y, Zhang M, Wang C (2020) Mechanistic insights into the interactions of dynein regulator Ndel1 with neuronal ankyrins and implications in polarity maintenance. *Proc Natl Acad Sci U S A* 117: 1207–1215
- Yoshimura T, Rasband MN (2014) Axon initial segments: diverse and dynamic neuronal compartments. *Curr Opin Neurobiol* 27: 96–102
- Zhao Y, Wu X, Chen X, Li J, Tian C, Chen J, Xiao C, Zhong G, He S (2020) Calcineurin signaling mediates disruption of the axon initial segment cytoskeleton after injury. *iScience* 23: 100880
- Zhou B, Yu P, Lin MY, Sun T, Chen Y, Sheng ZH (2016) Facilitation of axon regeneration by enhancing mitochondrial transport and rescuing energy deficits. *J Cell Biol* 214: 103–119



License: This is an open access article under the terms of the [Creative Commons Attribution-NonCommercial-NoDerivs](https://creativecommons.org/licenses/by-nc-nd/4.0/) License, which permits use and distribution in any medium, provided the original work is properly cited, the use is non-commercial and no modifications or adaptations are made.

Expanded View Figures

Figure EV1. Injury-induced *Atf3*:BAC2 Tg mouse and *Rpt3* CKO mouse.

- A Time-dependent GFP expression in injured hypoglossal motor neurons of *Atf3*:BAC2 Tg mouse at 20, 36, and 48 h after injury.
- B Representative image stained by ATF3 and GFP antibodies at 5 days following hypoglossal nerve injury of *Atf3*:BAC2 Tg mouse.
- C The graph showing the percentage of GFP (+) or GFP (–) hypoglossal MNs in ATF3(+) MNs of control and injured sides at 5 days after injury of *Atf3*:BAC2 Tg mouse ($n = 3$ mice).
- D Schematic of the breeding strategy to generate injury-induced *Rpt3* CKO mouse.
- E Diagram for *Atf3*:BAC2 transgene and *Rpt3* gene. Arrows indicate the location of the genotyping primers (1)–(5) for *Atf3*:BAC2 Tg and *Rpt3* CKO mouse. The gray triangles show loxP sites.
- F Representative genotyping results using primers (1)–(4) to obtain *Rpt3* CKO mouse. PCR products on the gel are amplified using indicated primer pairs.
- G Representative genotyping using tail samples of adult *Rpt3* CKO mice from #1 to #4 shows that the floxed *Rpt3* alleles are not deleted.

Data information: Dashed lines outline hypoglossal nucleus in (A and B). XII, hypoglossal nucleus; cc, central canal. Scale bars, 150 μ m in (A and B).

Source data are available online for this figure.

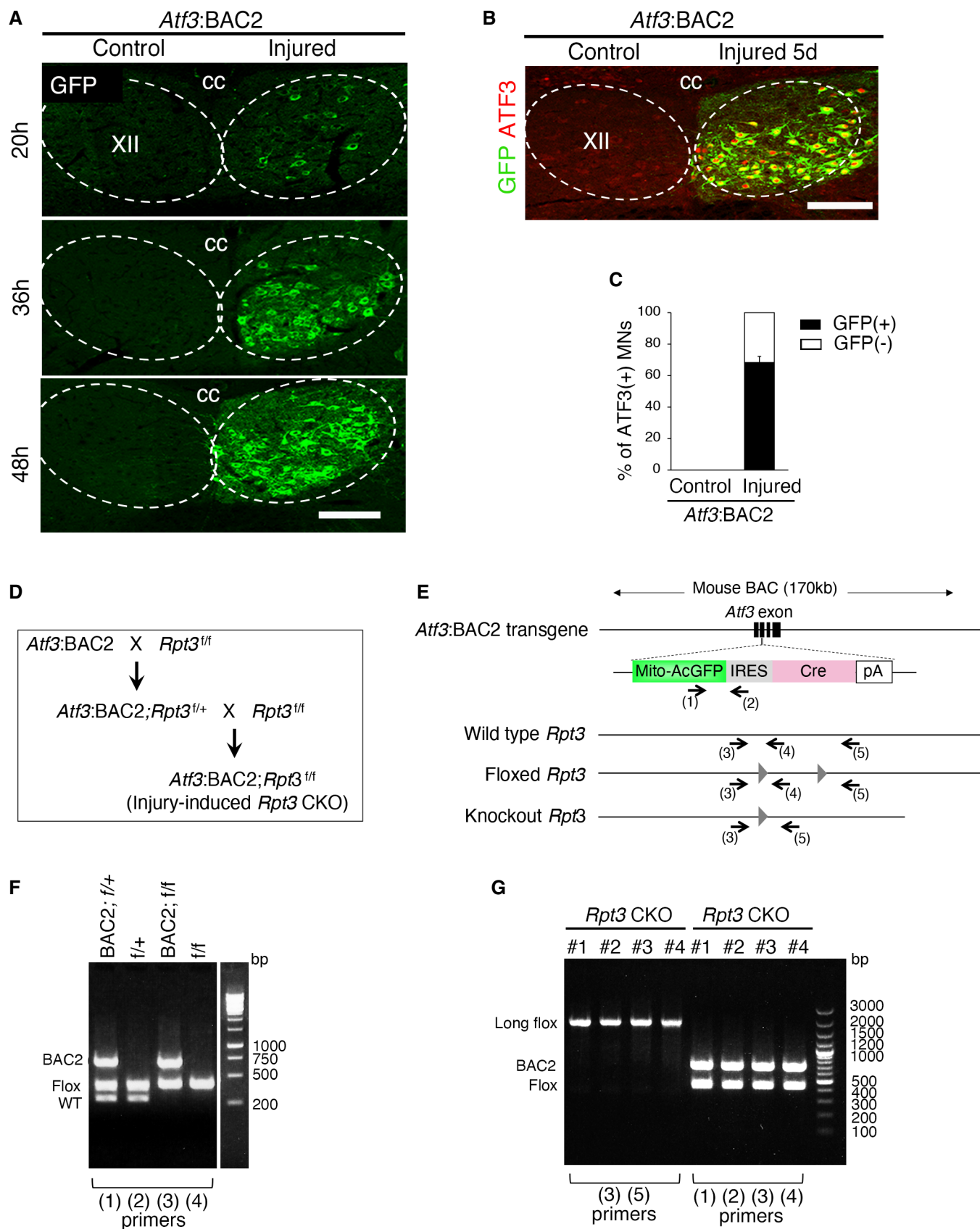


Figure EV1.

Figure EV2. GFP-labeled mitochondria in injured hypoglossal motor neurons of *Atf3:BAC2* Tg and *Rpt3* CKO mice.

- A Whole-mount observation of hypoglossal nerve of *Atf3:BAC2* Tg mouse without staining.
- B Immunostaining of hypoglossal nerve at 5 and 10 days after injury, using anti-GFP, Lamp1, and neurofilament (NF) antibodies. Arrows show Lamp1 positive signals in injured nerve.
- C Graph shows mitochondria number in hypoglossal (XII) axon at 5 days and 10 days after injury ($n = 4$ mice).
- D Graph shows lysosome number in hypoglossal (XII) axon at 5 days and 10 days after injury ($n = 4$ mice).
- E The GFP expression of injured hypoglossal motor neurons at 5 days following injury. XII, hypoglossal nucleus; cc, central canal.
- F The percentage of GFP-positive injured motor neurons compared with ChAT-positive uninjured motor neurons ($n = 3$ mice per group).
- G Super-resolution images of GFP-stained mitochondria in injured hypoglossal motor neuron. Stacked image of 2 μm thickness.
- H Single layer image corresponding to boxed area in (G) and plot profile of the fluorescence intensity corresponding to the line in the image.

Data information: Dashed lines outline axon in (A) and hypoglossal nucleus in (E). Data are shown as the mean \pm s.e.m. $*P = 0.0247$, $**P = 0.0011$ in (C), $***P < 0.0001$ in (D), $P = 0.7854$ in (F), determined by one-way ANOVA followed by *Tukey post hoc* test. Scale bars, 300 μm in (A; left two panels) and 10 μm in (A; right panel), 5 μm in (B), 150 μm in (E), 4 μm in (G), and 2 μm in (H).

Source data are available online for this figure.

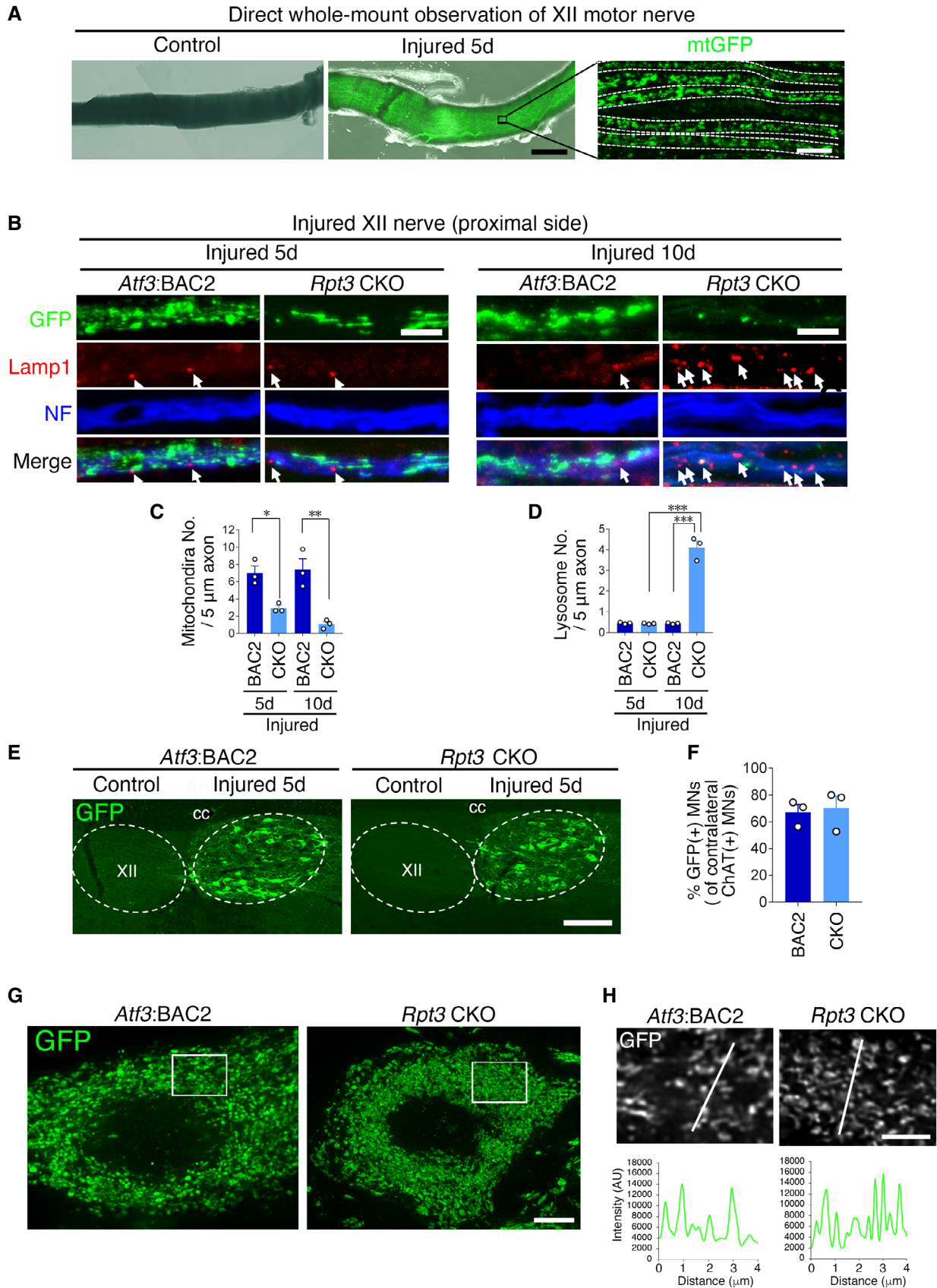


Figure EV2.

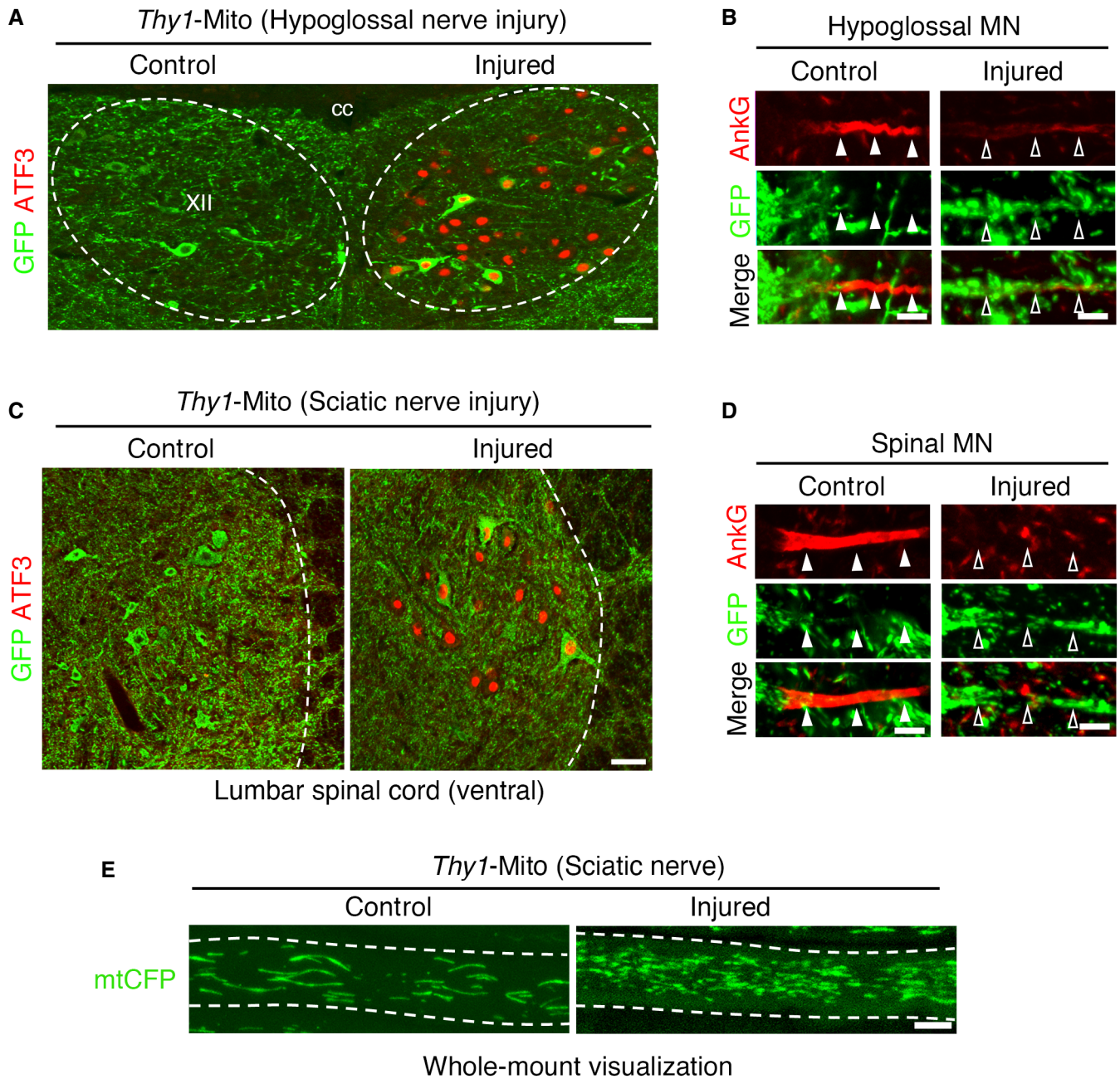


Figure EV3. Expression of CFP-labeled mitochondria in *Thy1-mito*-CFP Tg (*Thy1-Mito*) mouse before and after motor nerve injury.

- A Immunostaining of hypoglossal nucleus (XII) of *Thy1-Mito* mouse using ATF3 (red) and GFP (green) antibodies at 5 days following hypoglossal nerve injury. XII, hypoglossal nucleus; cc, central canal.
- B The localization of AnkG and CFP-labeled mitochondria in the AIS of uninjured and injured hypoglossal motor neurons of *Thy1-Mito* mouse.
- C Immunostaining of the lumbar spinal motor neurons of *Thy1-Mito* mouse using ATF3 (red) and GFP (green) antibodies at 5 days following sciatic nerve injury.
- D The localization of AnkG and CFP-labeled mitochondria in the AIS of uninjured and injured spinal motor neurons of *Thy1-Mito* mouse.
- E Whole-mount observation of CFP-labeled mitochondria (mtCFP) in sciatic nerve.

Data information: Dashed lines outline hypoglossal nucleus (A), spinal cord (C) and axon (E). Closed arrowheads indicate the AIS, while open arrowheads indicate the region where the AIS is disrupted in (B and D). Scale bars, 50 μ m (A and C) and 5 μ m (B, D and E).

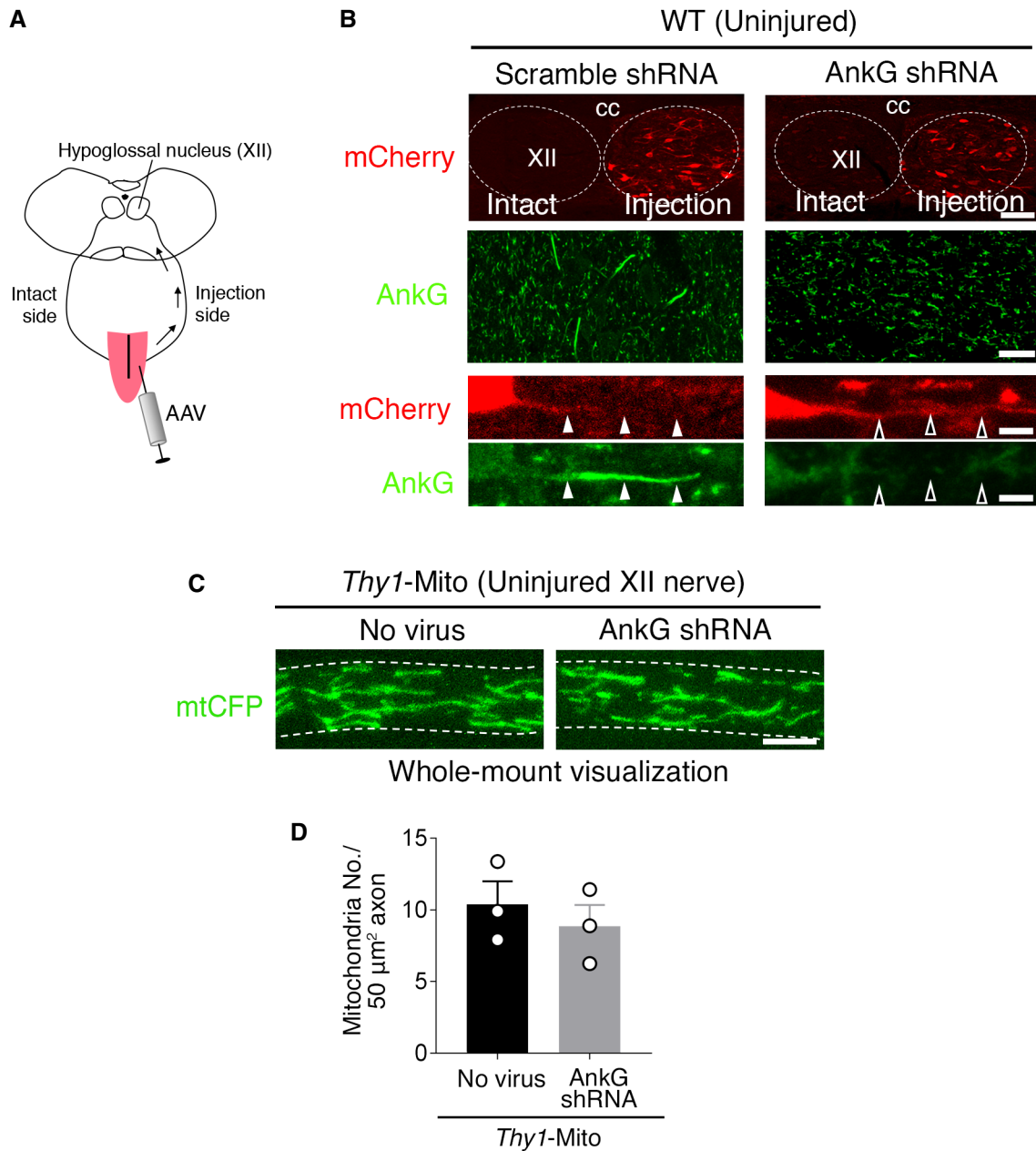


Figure EV4. Suppression of AnkG in uninjured hypoglossal motor neurons.

A Schematic diagram for AAV injection to tongue.

B Hypoglossal motor neurons labeled by mCherry (red) in injection side of AAVs. The decrease of AnkG (green) immunoreactivity is observed after the infection of AAV-AnkG shRNA but not AAV-scramble shRNA. Dashed lines show hypoglossal nucleus (XII). cc, central canal. Closed arrowheads indicate the AIS, while open arrowheads indicate the region where the AIS is disrupted.

C CFP-labeled mitochondria in uninjured hypoglossal nerve of *Thy1-Mito* mouse after the infection of AAV-AnkG shRNA to tongue. Dashed lines show axon.

D Graph shows the number of CFP-labeled mitochondria in uninjured hypoglossal (XII) axon of *Thy1-Mito* mouse before and after AAV infection. Data are shown as the mean ± s.e.m. (no significant difference ($P = 0.519$), determined by two-tailed Student's *t*-test, $n = 3$ mice).

Data information: Scale bars = 100 μm (top), 20 μm (middle), and 5 μm (bottom) in (B) and 5 μm in (C). Source data are available online for this figure.

Figure EV5. Characterization of *Atf3*:BAC;*SOD1*^{G93A} (*Atf3*;*SOD1*) mouse.

- A Schematic of the breeding strategy to generate *Atf3*;*SOD1* mouse.
- B Kaplan–Meier survival analysis (long-rank test, $P = 0.4674$). The *Atf3*:BAC transgene has no significant effect on life span of *SOD1*^{G93A}.
- C Representative image of spinal motor neurons at 45, 70, and 130 days, immunostained with ChAT.
- D Quantification of age-dependent ChAT-positive MN in the ventral horn of lumbar spinal cord. Data are shown as the mean \pm s.e.m., no significant differences at same age, determined by unpaired *t*-test, $n = 3$ mice per group.
- E The expression of GFP and ChAT in spinal motor neurons of *Atf3*;*SOD1* at 45, 60, 90 and 130 days.
- F The percentage (%) of GFP-positive MNs (black bar) of ChAT-positive MNs in *Atf3*; *SOD1* mice. Data are shown as the mean \pm s.e.m. $n = 5$ mice at each age.
- G Immunostaining of spinal motor neurons in *Atf3*;*SOD1* at P65 using GFP, MMP-9, OPN, and ChAT antibodies. Arrows denote GFP-positive motor neurons co-localized with MMP-9 or OPN.

Data information: Scale bar, 100 μ m in (C), 50 μ m in (E), and 20 μ m in (G).

Source data are available online for this figure.

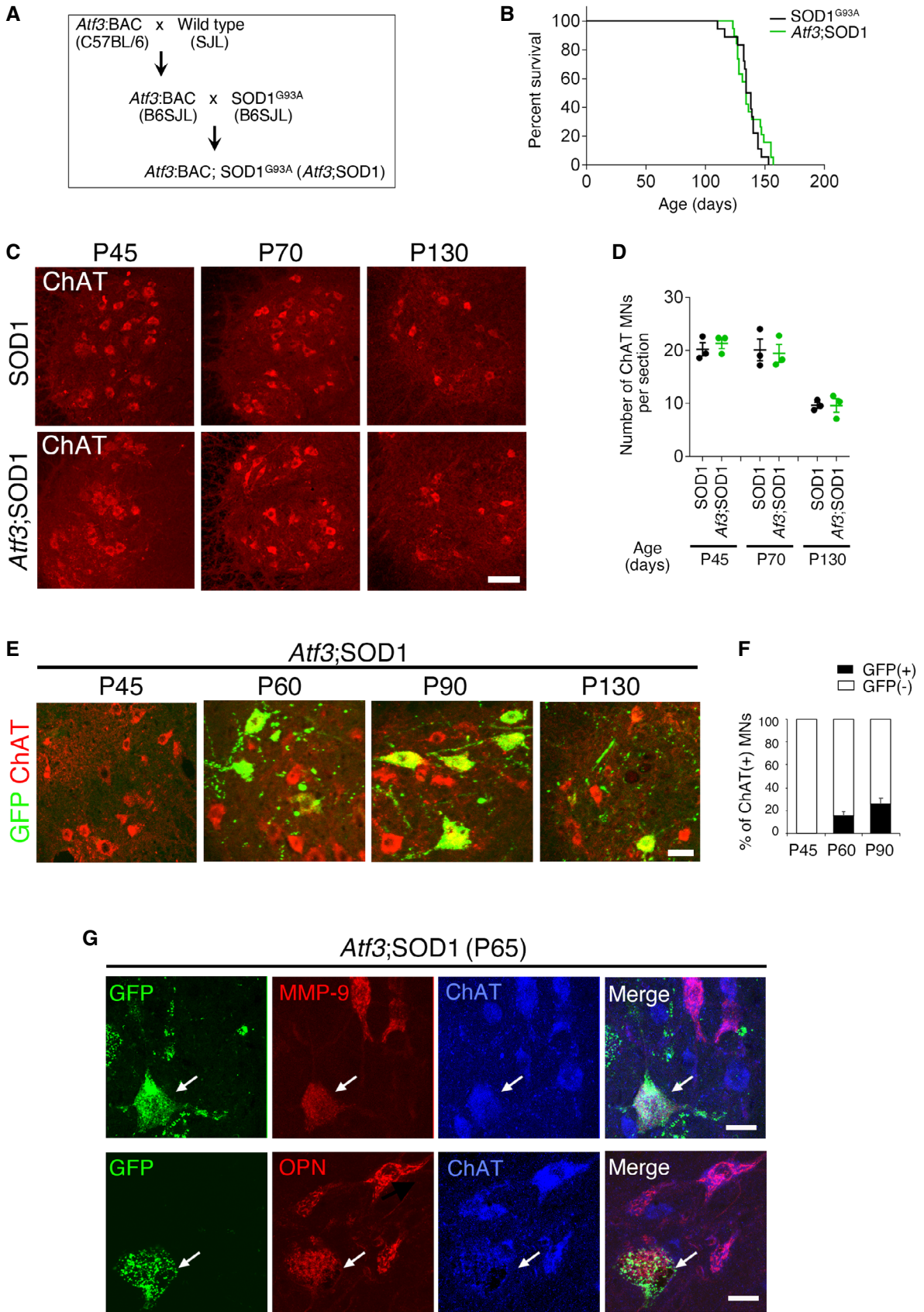


Figure EV5.

Mitochondrial entry into damaged axons is restricted by impaired disassembly of the axon initial segment

Sumiko Kiryu-Seo, Reika Matsushita, Yoshitaka Tashiro, Takeshi Yoshimura, Yohei Iguchi, Masahisa Katsuno, Ryosuke Takahashi, Hiroshi Kiyama

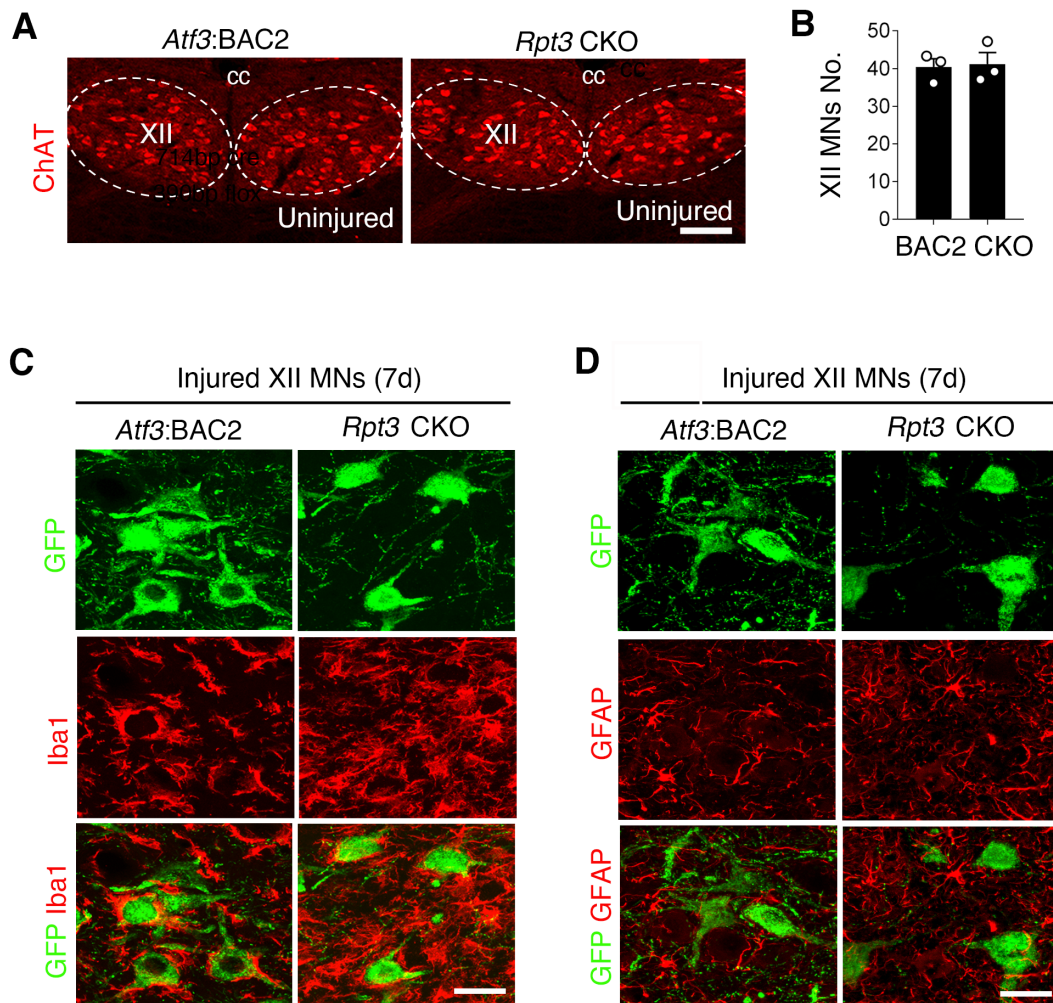
Table of contents

Appendix Figure S1: Hypoglossal motor neurons and glial cells of *Atf3*:BAC2 Tg and *Rpt3* CKO mice before and after nerve injury

Appendix Figure S2: The expression of GFP and AnkG in spinal motor neurons of *Atf3*:BAC2 Tg and *Rpt3* CKO mice after sciatic nerve injury

Appendix Figure S3: The GFP-labeled hypoglossal motor neurons in *Atf3*:BAC;SOD1 mouse

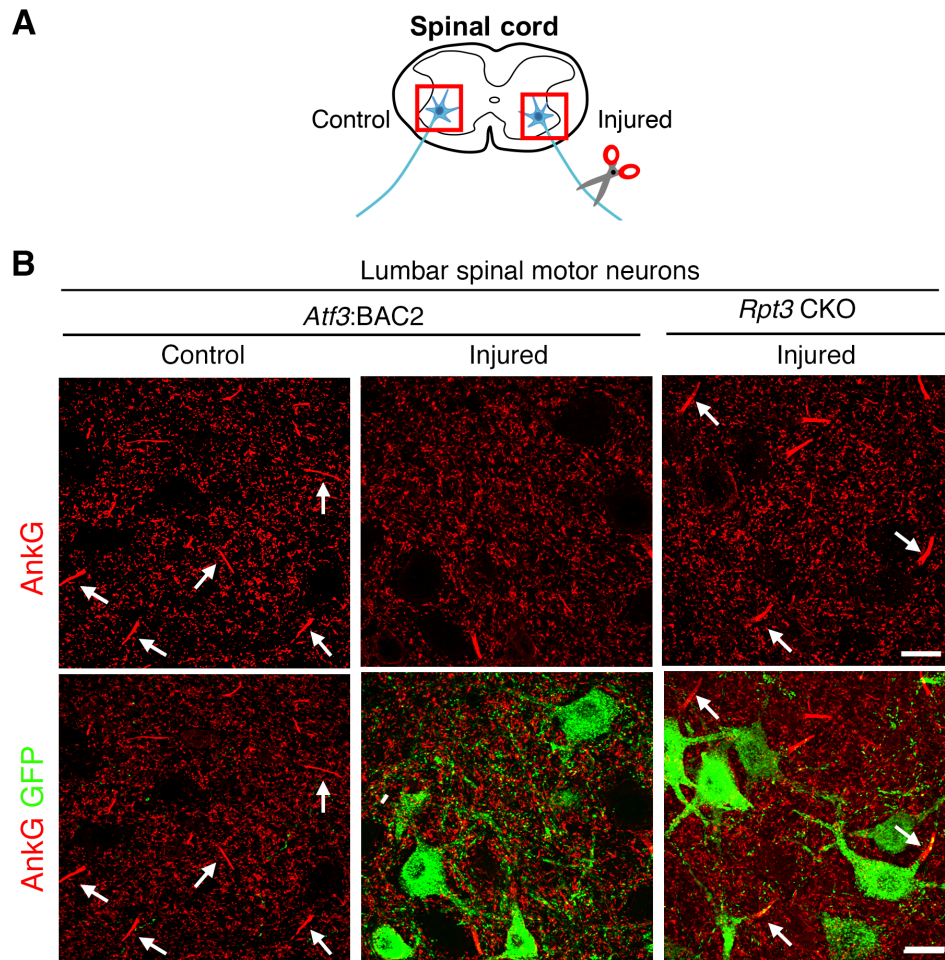
Appendix Table S1 : Primer list



Appendix Figure S1: Hypoglossal motor neurons and glial cells of *Atf3*:BAC2 Tg and *Rpt3* CKO mice before and after nerve injury.

- A.** Uninjured hypoglossal nucleus immunostained by anti-ChAT antibody. XII, hypoglossal nucleus; cc, central canal; MNs, motor neurons. Dashed lines outline hypoglossal nucleus
- B.** The graph showing the number of motor neurons in unilateral hypoglossal nucleus per section. Data are shown as the mean \pm s.e.m. and no significance, determined by Student's *t*-test ($n=3$ mice per group).
- C.** Injured hypoglossal nucleus at 7 days after injury, immunostained by anti-GFP and -Iba1 antibodies. Microglial cells are more activated around injured hypoglossal motor neurons (MNs) of *Rpt3* CKO mouse.
- D.** Injured hypoglossal nucleus at 7 days after injury, immunostained by anti-GFP and -GFAP antibodies.

Scale bars, 150 μ m in (A) and 30 μ m in (C and D).

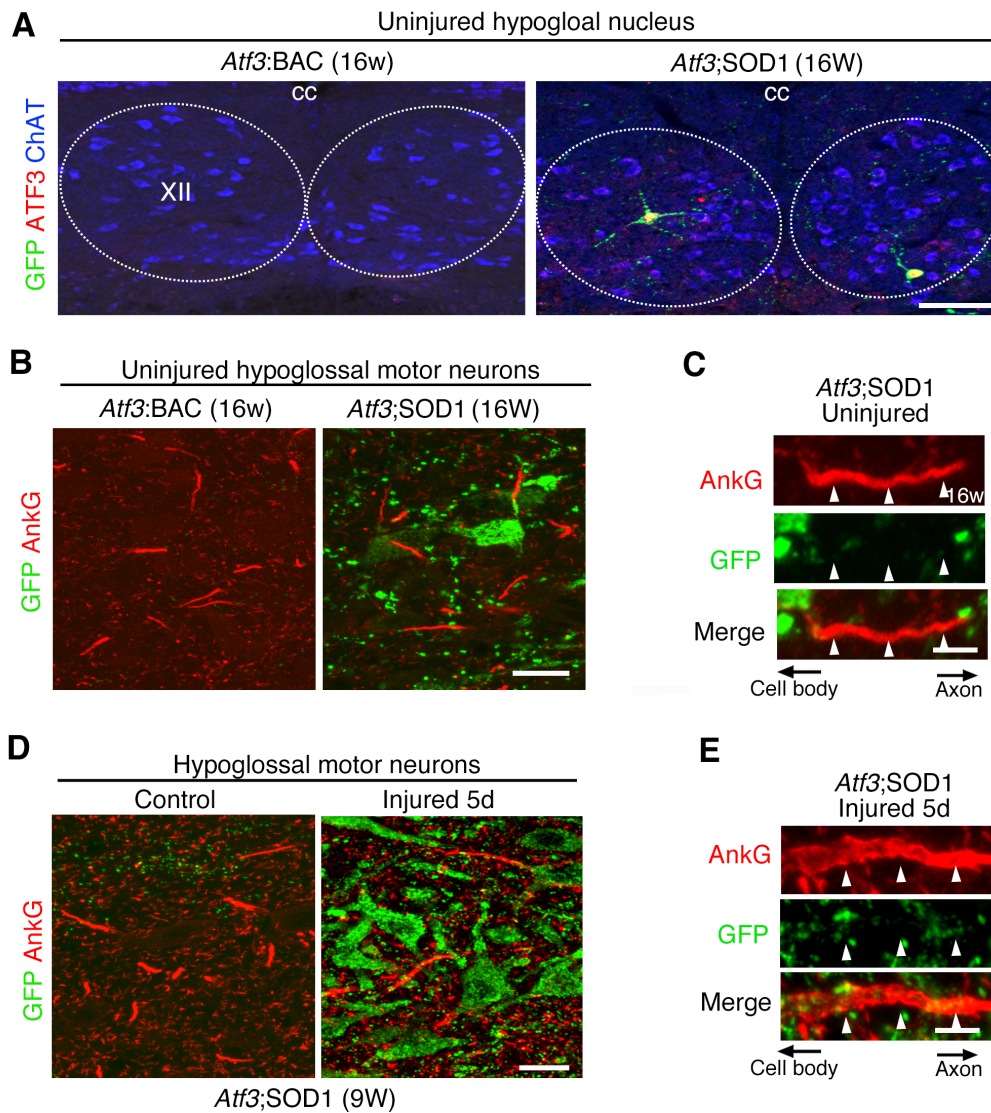


Appendix Figure S2: The expression of GFP and AnkG in spinal motor neurons of *Atf3*:BAC2 Tg and *Rpt3* CKO mice after sciatic nerve injury.

A. Schematic diagram of sciatic nerve injury model. The area surrounded by red box is observed in (B).

B. Spinal motor neurons of *Atf3*:BAC2 Tg and *Rpt3* CKO mice before and at 5 days after injury, immunostained for AnkG and GFP. Arrows indicate the AIS stained by AnkG.

Scale bar, 30 μ m.



Appendix Figure S3: The GFP-labeled hypoglossal motor neurons in *Atf3*;SOD1 mouse.

- A.** Uninjured hypoglossal motor neurons of *Atf3*;SOD1 mouse at 16 weeks old, immunostained by GFP, ATF3 and ChAT. Dashed lines outline hypoglossal nucleus (XII). cc, central canal.
- B.** Uninjured hypoglossal motor neurons of *Atf3*;SOD1 mouse at 16 weeks old, immunostained by AnkG- and GFP- antibodies.
- C.** The localization of the AIS and mitochondria in uninjured GFP-positive motor neurons of *Atf3*;SOD1 mouse at 16 weeks old.
- D.** Hypoglossal motor neurons of *Atf3*;SOD1 mouse (9 weeks old) at 5 days after injury, immunostained by AnkG- and GFP- antibodies.
- E.** The localization of AnkG and GFP-labeled mitochondria in the AIS of uninjured and injured hypoglossal motor neurons of *Atf3*;SOD1 mouse at 9 weeks old. Arrowheads indicate the AIS.
- Scale bars, 100 μ m in (A), 20 μ m in (B and D), 5 μ m in (C and E).

Appendix Table S1: Primer list

Oligonucleotides	
Sprr1a-S	TTGTGCCCCCAAACCAAG
Sprr1a-A	GGCTCTGGTGCCTTAGGTTG
Atf3-S	ATGTCAGTCACCAAGTCTGAGGC
Atf3-A	TGGATAAAGAGGTTCTCTCGTCTTCC
Gadd45a-S	CTGCTGCTACTGGAGAACGAC
Gadd45a-A	CGACTTTCCCGGCAAAAACAAA
Cd44-S	CACCATTGCCTCAACTGTGC
Cd44-A	TTGTGGGCTCCTGAGTCTGA
Fos-S	CCATGATGTTCTCGGGTTTC
Fos-A	TGTCACCGTGGGGATAAAGT
Gap43-S	TGGTGTCAAGCCGGAAGATAA
Gap43-A	GCTGGTGCATCACCCCTTCT
Sox11-S	CGACGACCTCATGTTTCGACC
Sox11-A	GACAGGGATAGGTTCCCCG
Smad1-S	GCTTCGTGAAGGGTTGGGG
Smad1-A	CGGATGAAATAGGATTGTGGGG
Dine-S	GTCTCTGAACTACGGGGGTATTGGCAC
Dine-A	GTAGGCCAGCTTGAGGCCTCCCATGTC
Rbfox3-S	ATCGTAGAGGGACGGAAAATTGA
Rbfox3-A	GTTCCCAGGCTTCTTATTGGTC
Gapdh-S	GGTGAAGGTCGGTGTGAACG
Gapdh-A	CGTGAGTGGAGTCATACTGGA
Pan AnkG-S	CTAGAGTCCCCAGCGCAAGCTCG
Pan AnkG-A	GCCTTTGCTTCTGGAATGACTTCCG
Giant AnkG-S	CGAGTTCACATCTAAGACACCA
Giant AnkG-A	TCACGATCTGTTTCCTTCTCC
Chat-S	GACCAGCTAAGGTTTGCAGC
Chat-A	CAGGAAGCCGGTATGATGAGA
Genotyping primers	
primer (1)	CAATAAGATGGAGTACAACACTACAACGC
primer (2)	GACTCTTTCCACAACACTATCCAACCTCAC
primer (3)	TGAGCTGTGTATCAAGGTCC
primer (4)	TAGAAGCTGCCTAAGGCACA
primer (5)	TGCAATCCCTTGTGAGGAGA